MDPI

Review

Methods for quantifying expansion in lithium-ion battery cells resulting from cycling: a review

Tessa Krause [1,2,†,*], Daniel Nusko[3,†], Luciana Pitta Bauermann [3,*], Matthias Vetter [3], Marcel Schäfer [2], and Carlo Holly [1,4]

[1] RWTH Aachen University TOS – Lehrstuhl für Technologie Optischer Systeme, Steinbachstraße 15, 52074 Aachen, Germany
[2] Precitec GmbH & Co. KG, Draisstraße 1, 76571 Gaggenau, Germany
[3] Fraunhofer Institute for Solar Energy Systems ISE, Heidenhofstr. 2, 79110 Freiburg, Germany
[4] Fraunhofer Institute for Laser Technology ILT, Steinbachstraße 15, 52074 Aachen, Germany
* Correspondence: t.krause@precitec.de (T.K.), luciana.pitta.bauermann@ise.fraunhofer.de (L.P.B.)
† These authors contributed equally to this work.

Abstract: Significant efforts are being made across academia and industry to better characterize lithium-ion battery cells as reliance on the technology for applications ranging from green energy storage to electric mobility increases. The measurement of short-term and long-term volume expansion in lithium-ion battery cells is relevant for several reasons. For instance, it provides information about the quality and homogeneity of battery cells during charge and discharge cycles, as well as aging over it's lifetime. The expansion measurements are useful for the evaluation of new materials and the improvement of end-of-line quality tests during cell production. These measurements may also indicate the safety of battery cells by aiding in predicting state of charge and state of health over the lifetime of the cell. Expansion measurements can also assess inhomogeneities on the electrodes and defects such as gas accumulation and lithium plating. In this review, we first establish the known mechanisms through which short term and long term volume expansion in lithium-ion battery cells occurs. We then explore the current state-of-the-art for both contact and non-contact measurements of volume expansion. This review compiles existing literature to outline the various options available to researchers aiming to make *ex situ* volume expansion measurements by doing post mortem analyses on individual components and *in operando* measurements on entire battery cells. Finally, we discuss the different considerations when selecting an appropriate measurement technique. The selection of the optimal method for measuring battery cell expansion depends on the objective of the characterization, duration, required resolution, and repeatability of results. Costs and required space for the measurement equipment are also considered.

Keywords: lithium-ion; battery cells; expansion measurements; volume expansion; thickness changes

Citation: Krause, T.; Nusko, D.; Pitta Bauermann, L.; Vetter M.; Schäfer M.; Holly C. Methods for quantifying expansion resulting from cycling in lithium-ion cells: a review. *Energies* **2023**, *1*, 0. https://doi.org/

Received:
Revised:
Accepted:
Published:

1. Introduction

Due to ongoing concerns regarding climate change, many European governments have enacted legislation to stop or significantly reduce the production of internal combustion engine vehicles in the next few decades [1]. This is putting more pressure than ever on both academia and industry to develop energy storage solutions for electric vehicles that have suitable capacity and operational lifetime. At present, the most promising avenue for the electrification of the global vehicle fleet is lithium-ion battery technology. In addition, the adoption of green energy solutions, such as solar and wind power, necessitates energy storage solutions. Lithium ion battery technology is well suited to energy storage applications as well, as it has higher energy densities and faster charging than previously used battery technologies such as lead-acid, nickel-cadmium or nickel-metal hydrid cells [2].

New active materials are continuously being tested to enhance the performance and longevity of battery cells, while also improving sustainability, from both an economic and environmental perspective. Moreover, the manufacturing of lithium-ion battery cells is a complex, multi-step process, where each step must be executed with low tolerance for error to ensure short-term and long-term performance and safety [3]. As such, a number of metrology and measurement approaches are used to characterize various components in the battery cell. One important parameter to be measured is the reversible and irreversible expansion of the electroactive materials coated on both electrodes that occurs during charging and discharging cycles on assembled battery cells. Measuring expansion can be used to validate expansion models, such that manufacturers can predict how much a properly functioning battery cell will expand during its lifetime under normal operation conditions. This is particularly important when considering electric vehicles where hundreds, or sometimes thousands of cells are packaged tightly together. Should unexpected volume expansion occur, the individual cells might exert excessive pressure on each other, which could lead to failure modes with performance and safety consequences such as detachment of the electrical contact and poor heat dissipation among the cells. Expansion measurements can also be useful to assess the results of aging inside the battery cells such as gas and metallic lithium generation.

In this review, we explore the mechanisms for battery expansion, and the various technologies that are being reported across the literature to measure expansion in lithium-ion battery cells.

2. Expansion Mechanisms in Battery Cells

Different mechanisms are responsible for the expansion of battery cells during cycling. Expansion mechanisms can be divided into either reversible or irreversible manifestations [4,5]. Reversible expansion occurs due to the intercalation of lithium-ions into and out of the electrodes [6]. Conversely, due to irreversible expansion the thickness of the battery cell does not return to the initial state and indicates degradation over its lifetime [7–9]. The main causes of irreversible expansion are the further formation of the solid-electrolyte-interphase (SEI) layer, lithium plating and gas formation [9–11].

2.1. Reversible Expansion

The main expansion mechanism in lithium-ion batteries is the so called "rocking-chair mechanism". The lithium ions stored in the lattice of the electrodes are transported from the negative to the positive electrode by diffusion during discharge, with the reverse occurring during charging. This principle is shown in Figure 1. The electrodes go through a reversible swelling and contraction phases during charge and discharge due to the intercalation of lithium-ions [12–15].

2.1.1. Anodes

The negative electrode, commonly referred to as the anode, is typically composed of a copper current collector coated with electroactive materials and additives [17]. The most common anode material in modern lithium-ion batteries is graphite. It has a maximum gravimetric capacity of 372 mAh/g while storing one lithium-ion per six carbon atoms in its fully lithiated stage (LiC_6) [18,19]. Figure 2 shows the open circuit voltage (OCV) of graphite and the stages from unlithiated carbon to fully lithiated. Through intercalation in the charging process, lithium ions are extracted from the lithium metal oxide in the cathode and are inserted into the graphite host lattice of the anode. The intercalation of the lithium ions occurs through different stages. Unlithiated graphite, C_6, initially stores lithium ions in stage 1L with a small amount of lithium randomly distributed in the graphite host lattice, creating a solid-solution [20]. In stage 4, every fourth graphite layer is completely filled with lithium ions. Stage 3 is formed with further lithiation and one additional filled layer, where now every third layer is filled. In the transition phase from stage 2 L to stage 2, one additional layer is filled. At stage 2, every second layer is completely filled. The transition

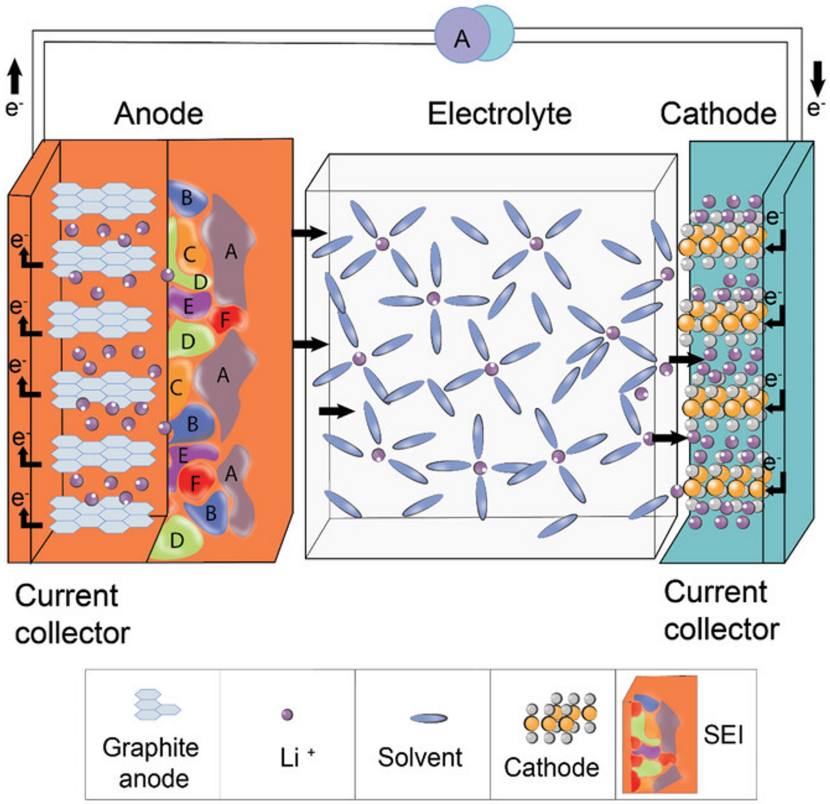

Figure 1. Illustration of the components and working principle of lithium-ion battery cells; Reproduced under Creative Commons License without any changes (CC BY-NC-ND 4.0 by Adenusi et al. [16])

from stage 2 to stage 1 requires six further layers to be filled. In the dense stage 1, every layer between two graphite layers is filled with lithium [21,22]. During intercalation into the graphite anode, an expansion of up to 10 % has been observed [23,24]. The typical plateau in Figure 2 from stage 2L to stage 2 depends on the phase transition inside the lattice. Stage 2L is not ordered, the lithium ions in the anode are in undefined positions. Only after reaching stage 2 are all positions filled. Therefore, there is no expansion in this phase, only an ordering of the ions. Stage 2L only appears during delithiation (discharge) and stage 3 appears during lithiation (charge) and forms directly into stage 2 [25]. During deintercalation, the lithium ions are extracted randomly out of the structure, which forms a solid solution or a liquid, rather than a sorted phase [26].

While graphite is the most prevalent, other materials are utilized as an anode for lithium-ion battery cells. One such material is Lithium-Titanate (LTO). LTO has a very low gravimetric capacity of 175 mAh/g in comparison to graphite. During (de-)lithiation, three lithium-ions can intercalate into LTO with a average structure strain of approximately 0.2 %. This makes LTO a zero-strain material with high cycling stability [28]. Unlike graphite, in LTO anodes, there is no formation of a SEI passivation layer. This is due a to redox potential of 1.55 V vs. Li^+/Li. This negative electrode potential is higher than the reduction potentials of most electrolytes [29,30]. LTO anodes have the advantages of good cyclic performance, safe operation, high-power and almost no volume change during intercalation. However, LTO anodes suffer from a low electronic conductivity and lithium-ion diffusion coefficient, which leads to low charge and discharge capabilities in high C-rate conditions [31–33].

Silicon is also utilized as an anode material. Silicon (Si) has the highest theoretical gravimetric capacity among the current materials used as anode with up to 4,200 mAh/g [34]. This high capacity is possible due to the relatively large number of lithium ions per silicon atom. One silicon atom can host 4.4 lithium ions [35]. Due to the high density of intercalated lithium ions into the silicon, the volume expansion of the anode is substantial.

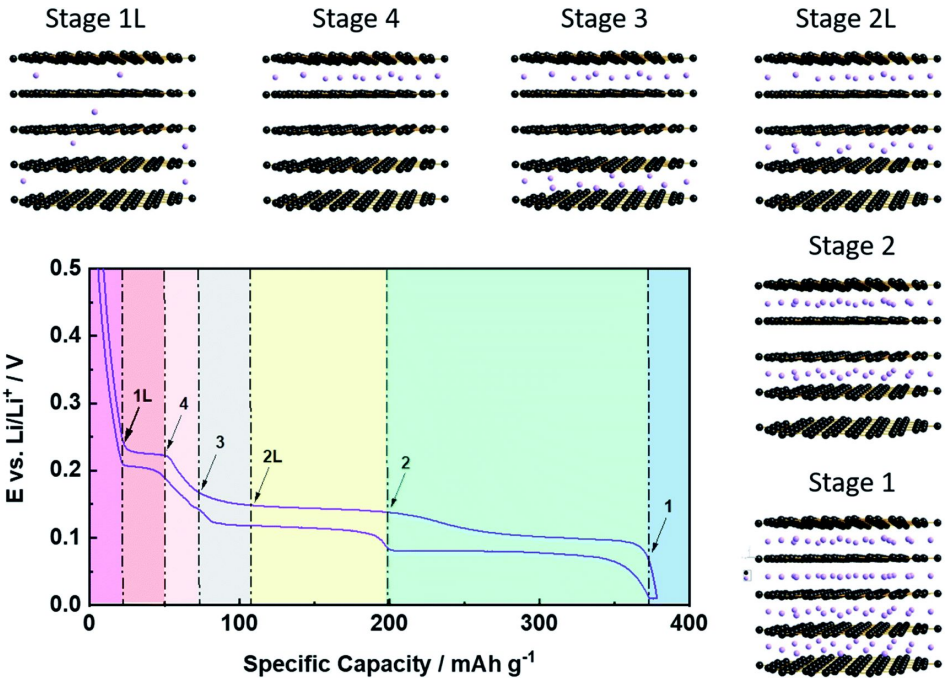

Figure 2. Graphite potential and schematic lithium (purple spheres) intercalation during (dis-) charging. The transition from stage 4 to stage 3 requires one out of six layers to be opened, the transition from stage 3 to stage 2 requires two out of six layers to be opened, and the transition from stage 2 to stage 1 requires three out of six layers to be opened. In dense layer 1, every layer is completely filled; Reproduced under Creative Commons License without any changes (CC BY 3.0 by Asenbauer et al. [27])

The anode expansion has been observed to be from 280 % up to more than 300 % of its original thickness [36–39]. Significant expansion can lead to cracks in the SEI layer, which can cause redox reactions between the electrolyte and the electrode's active material. These reactions can induce loss of active material (LAM), leading to loss of capacity [40]. Alloys of graphite and silicon are used as an anode to combine the benefits of both materials [41]. The alloy formation occurs during lithiation and thus reduces charge and discharge rates. The pore size into which the lithium ions can intercalate also plays a key role in the magnitude of possible C-rates. In high energy battery cells, the anode pore size is smaller than in standard designs. In such battery cells, high charge or discharge rates can lead to the formation of irreversible lithium plating. [42]

2.1.2. Cathode

The positive electrode in a lithium-ion battery, often referred to as the cathode, is the most dominant factor in determining its working potential range. Most anode potentials lie at around 0.5 V vs. Li/Li^+ [15]. As a primary cathode material, lithium-cobalt-oxide (LCO) or Li_xCoO_2 has become widely accepted for use in electronic devices [43]. This material has a relatively high specific capacity of approximately 140 mAh/g for $x = 0.5$. The theoretical capacity of up to 270 mAh/g at $x = 1$ is not maintainable over repeated cycling. Oxygen reduction and electrolyte decomposition could lead to thermal runaway [15]. The expansion of a LCO cathode is around 1.8 % of the initial thickness [44].

The most common cathode materials for use in electric vehicles (EVs) are nickel-mangan-cobalt (NMC) or $LiNi_{1-x-y}Co_yMn_xO_2$ and nickel-cobalt-aluminium (NCA) or $LiNi_{1-x-y}Co_xAl_yO_2$ (with $x + y < 0.1$) [43,45]. The specific capacity of NMC as cathode material is 160 mAh/g to 175 mAh/g [46]. The swelling and contraction of the cathode due to intercalation is typically at least 1 % to 3 % [47] and up to 4.5 % [48] of the initial volume, for NMC and NCA respectively. NMC cathodes are advantageous due to their enhanced

specific capacity, thermal stability and the possibility to have different quantity shares of individual materials (x,y) [49].

Another common cathode material is lithium iron phosphate (LFP) or ($LiFePO_4$). The theoretical volume change of this material between complete charge and discharge is 6.8 % from the initial volume. An important advantage of LFP batteries is their long lifetime of up to 6,000 cycles, roughly three times higher than NMC cells. Unfortunately, the material has low conductivity, low lithium-ion diffusion coefficient, high self-discharge rates and, compared with other materials, a relative low specific capacity of 130 mAh/g to 140 mAh/g [49,50].

2.1.3. Thermal Expansion

Variation in the internal temperature of battery cells might trigger thermal runaway and capacity fade, and also induce internal mechanical stress [51]. This internal stress is a safety issue during the operation of the cell. Heat production in battery cells can be divided into two different internal heat sources: Joule heat, and heat generated through entropy changes due to chemical reactions [52].

Joule heat is generated by the Ohmic resistance of the electrically conductive internal components, such as the electrodes, through which electric current flows [53,54]. Internal resistance of a battery cell is assumed to be the limited ion and electron conductivity through the current collectors, the active materials, the connectors and the electrolyte [55]. The generated friction during electric flow is entirely transformed into heat. Therefore, the heat production due to Joules heat is completely irreversible and happens during both charging and discharging [56,57]. Differences in the Joule heat production and the thermal expansion due to the different thermal and electrical conductivity exists also in the external interface of the battery cell, the tabs [58]. At high discharge rates, the expected heat generation will occur near the positive tab. Typically, the collector used for the positive electrode is made of aluminum and the negative electrode is either made of copper or nickel. As a result, the positive electrode has poor thermal conductivity.

Entropy heat is a reversible heat production process in a battery cell. Entropy occurs due to the entropy change during electrochemical reactions from Gibbs free energy conversion to electrical energy. Since lithium-ion batteries have high specific energies, the Gibbs energy is high as well [57,59]. Heat generation due to entropy changes occurs exothermically during discharge and endothermically during charge, also contributing to reversible expansion. The components of the battery cell will expand and contract according to their dilatation coefficient. [53]

2.2. Irreversible Expansion

When a battery cell expands irreversibly, decomposition material is formed and the cell does not return to its initial form. This kind of thickness change is associated with cell degradation, such as gas generation, lithium plating, formation of SEI-layer or delamination of active materials due to insufficient external contraction after its expansion [60].

2.2.1. Solid-Electrolyte-Interface Layer

Most electrolytes are unstable at the operating potentials of common anode materials like graphite or silicon [61]. Since most electrolytes have decomposition potentials below 1 V vs. Li^+/Li, stable operation of the combination of negative electrode and electrolyte is not possible [62,63]. During the formation process of battery cells, a solid, electrically insulating boundary layer at the interface between the electrolyte and negative electrode is formed [64,65]. This layer is referred to as the SEI-layer. The nature of the SEI-layer is complex and not completely understood, but regardless, is one of the most important production step for the safe use of lithium-ion batteries. The generation of the SEI-layer occurs from the decomposition of electrolyte at the boundary of electrode/electrolyte [16,66]. The SEI-layer is mostly composed of inorganic materials such as Li_2CO_3, LiF, Li_2O and organic materials like carbonates and polyolefins [66,67]. At the electrode interface,

mostly inorganic and thermodynamically stable products are formed, whereas organic compounds are formed on the boundary facing the electrolyte [16]. The SEI-layer is shown in Figure 1 between the anode and the electrolyte as letters A to D. The consumption of electrolyte and active electrode material results in an irreversible capacity loss of the battery cell [66]. Once an initial and stable SEI layer has been formed, electrolyte can no longer be positioned adjacent to the electrode material and no further decomposition takes place. The lithium ions can, however, diffuse through the SEI-layer [68].

Since silicon undergoes a large expansion of up to 300 % of the original volume, there is a high risk that the SEI-layer is damaged during charging and discharging cycles. During lithiation, SEI-layer, which forms on the silicon particles, can break and a new interphase is created between the electrolyte and the electrode. This leads to a newly formed SEI-layer at the boundary, which, after many cycles, results in a irreversible expansion of the anode, irreversible loss of lithium inventory (LLI), and a capacity fade [67].

2.2.2. Lithium plating

Generally, modern lithium-ion battery cells do not contain any metallic lithium. The intercalation speed, with which lithium ions intercalate from the active materials of the cathode to the anode is dependent on the conditioning temperature. If the temperature during charging falls below 10 °C, a decrease in the nominal charge rate is to be expected [69]. Since the intercalation speed is limited, lithium ions might be deposited on the outer surface of the anode and be reduced to metallic lithium, referred to as lithium plating. Plating can occur when the anode potential falls below 0 V vs. Li/Li^+, and at low temperatures in combination with a high state of charge (SoC) and high charging rates [70,71]. Lithium plating is a critical safety issue. These electric conductive materials have the ability to pierce the separator and reach the opposite electrode causing a short circuit within the battery cell. Degradation effects such as LLI, LAM, and loss of electrolyte are also possible. Dead lithium, the main component of inactive lithium, on the anode surface can also form a electrically-insulating, high impedance layer [72]. All these degradation effects result in a reduction of the capacity of the battery cell [72].

Lithium plating can be divided into reversible and irreversible. The irreversible plating can react with the electrolyte resulting in the formation of the SEI-layer. It is also possible that some metallic lithium can intercalate as lithium ions into the anode host lattice after a certain relaxation time. This leads to a reversible lithium plating with a capacity recovery. [73,74]

2.2.3. Gas Generation

The first charge cycles of a battery cell during its manufacturing produces the controlled formation of the SEI-layer and gas generation by the decomposition of the electrolyte and electrode. Degassing is common practice in the cell manufacturing process. Further generation of gas can be a result of contamination within the cell, an incompatible combination of electrode/electrolyte materials, or due to abusive operating conditions (high/low temperature, under high pressure, or over/undercharging) [4]. Significant research has gone into additives to the electrolyte to prevent gas generation. The gas accumulation inside the cell can cause negative effects such as increased impedance between the electrodes, decreased capacity, shortened shelf life, and a shorter useful lifetime. In addition, this gas is usually composed of hydrogen or organic compounds which are often highly flammable [75]. Further formation of the SEI-layer due to degradation reactions leads to a production of gas which leads to irreversible swelling in battery cell. This reaction is exothermic and can cause an increase of the temperature inside the cell [52].

3. Measurement of expansion in lithium-ion battery cells

There are different approaches to measure the expansion in lithium-ion batteries. These can be divided into two groups: contact, and non-contact measurement approaches. The value of the expected expansion of battery cells depend on the chemistry used, thickness

and number of electrode layers. However, cell expansion should be in the range of a few micrometers to a few millimeters.

3.1. Contact approaches

Contact measurements can be carried out both outside the housing on entire battery cells and on individual components within disassembled battery cells. Contact measuring principles vary in terms of sensor contact area and the pressure applied between the sensor and object to be measured. Contact approaches can be divided into dilatometer, strain, and buoyancy measurements.

3.1.1. Dilatometer

Mechanical dilatometry is one of the oldest and most frequently used methods for measuring the expansion of different materials on a macroscopic level [76]. Primarily used to determine the specific temperature coefficient, this method has now become established for measuring the expansion of battery cells. The typical design of a dilatometer is comprised of a sensor that is positioned away from the heat source. As a result, it is possible to calculate the coefficient of thermal expansion (CTE) of the material or device by characterizing expansion [76].

Depending on the sensor design, dilatometers can be of various types, such as push piston, push rod, capacitance, high resolution-laser, and optical [77]. One of the advantages of dilatometer measurements is the possibility to measure the entire battery cell as well as single components individually. The advantage of dilatometry lies in its non-destructive nature and simplicity. The most common system, especially to measure the expansion of battery cells and electrochemical devices are push piston dilatometers [76,77]. The measuring object is placed between two plates, one fixed and one with the possibility to move parallel in the direction of the swelling.

Dilatometers can be used to make *ex situ* measurements to assess the expansion and the intercalation of guest ions into a host structure [78]. In this case, the battery cell must be disassembled and the thickness of individual components can be measured. For a good estimation of expansion in the battery cells, the post mortem analyses should be done for unaged and aged samples. In 1982 Biberacher et al. [79] presented a method for measuring the electrochemical intercalation of HSO_4^-/H_2SO_4 in graphite using a high-resolution push piston dilatometer. They observed a maximum dilation of 140 % for graphite during intercalation. Figure 3 shows two typical apparatuses for dilatometry measurements of electrochemical devices. Figure 3(**a**) shows the setup for the thickness measurement of single working electrodes. The working and counter electrodes are separated by a rigid separator, which is in modern dilatometer setups, typically made out of a stiff, but porous and permeable glass frit [80,81]. The push piston sensor is placed above the working electrode to measure the horizontal displacement from intercalation into, and deintercalation out of this electrode. The dilatometer illustrated in Figure 3 (**b**) has the ability to measure the swelling of whole battery cells. The displacement sensor is typically placed in the center of the battery cell.

Moyssari et al. [78] used an electrochemical dilatometer to measure the change in thickness of anode materials with different SiG compositions, one with a ratio of 0/95, and one with a ratio of 20/75. Two coin cells were made using each anode composition. The working electrode was SiG and the counter electrode was made of lithium metal. After a 6 h rest period, eight cycles were performed with a C-rate between 0.033 C and 0.1 C. The electrochemical dilatometer used contains a separator made of porous borosilicate glass between the two electrodes. This separator mechanically decouples the two electrodes. The expansion sensor applies a force of 1 N to ensure a permanent contact. It was found that the specific capacitance and the capacitance loss increase with higher silicon content. The hysteresis between lithiation and delithiation also increases with enlarged silicon content. During normal use, an expansion of 5.2 % occurs. Among other causes, this can be attributed to the continuous formation of SEI. In the formation cycles, the expansion

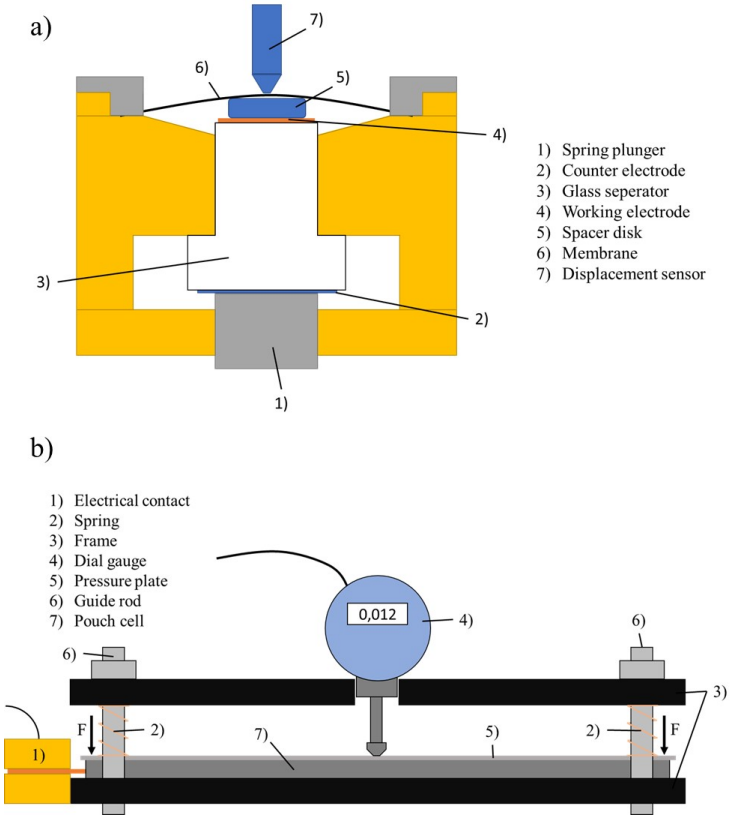

Figure 3. Two different dilatometer setups. a) Thickness measurement of a single working electrode with a stiff glass separator between both electrodes b) Typical *in-situ* dilatometry measurement of the whole cell on a macro scale. (Own representation based on a) [44,82] and b) [20,69])

behavior increased from about 5.5 % for the 0/95 electrode to about 47 % for the 20/75 electrode. For later cycles, the expansion behavior for the 0/95 electrode remains the same. For the next largest SiG ratio of 3/92, the expansion decreased from 14 % during formation to 7 % for further cycles. For the SiG ratio of 20/75 to a relative expansion of 20 % after the initial formation cycles. This expansion behavior remains constant during the further cycles, with little deviation. The specific capacity increases from a ratio of 0/95 to 20/75 from 326.55 mAh/g_{AM} to 925.62 mAh/g_{AM}. The authors also show that the lithiation of silicon takes place after the graphite lithiation is completed.

Rieger et al. [82] use dilatometry to investigate the expansion of commercially available LCO/G cells. For this purpose, one dilatometer was used for the graphite anode and one for the LCO cathode. The setup is similar to that shown in Figure 3 (**a**). Here, an expansion of the LCO cathode of about 2 % and of the graphite anode of about 7 % with complete lithiation were measured. During normal use, as specified by the manufacturer, there is an expansion of 5 %.

When the expansion of the entire battery cell is investigated, *in operando* measurements can be performed. The expansion of the complete battery cell is measured during charging and discharging cycles. The *in operando* measurement is included in the classification *in situ* measurements. The direct expansion at one point of the battery cell or at multiple points can be measured with linear displacement sensors as shown in Figure 3. The pressure that is built up due to the expansion inside the battery cell can also be measured with pressure sensors and load cells [83–86].

In Figure 3 (**b**) a common test stand for measuring the complete thickness change of battery cells is shown. Most of these setups consist of frames above and below the battery cell(3) held together by parallel screws (6). The battery cell (7) is typically placed on the bottom frame (3). A pressure plate (5) is placed on top of the cell, to create a constant

pressure over the entire surface. The swelling over the complete surface of the battery cell is measured. The screws also constrain the springs (2), which exert force on the pressure plate. The dial gauge (4) is located in the middle of the top frame. The electrical contact (1) is directly connected to a battery cell testing device. [20] Apparatuses similar to that in Figure 3 (**b**) were also used to investigate expansion in pouch cells in several references [20,48,52,69,87–95]. Some apparatuses exclude the springs (2) and pressure plate (5). In such cases, the expansion of a single point of an uncompressed battery cell is measured [96,97].

This apparatus allows for the measurement of the complete cell. The measurement of the complete battery cell gives information about all electroactive layers, separators and the electrolyte. In 2003, Lee et al. demonstrated one of the first test stands for the measurement of 1D battery expansion [98]. A data logger with a dial gauge was equipped to a constant load of 300 g. The dial gauge was connected to a data logger system and the complete rig was placed inside a climate chamber. The formation of the SEI layer in the initial charge was shown. The irreversible swelling was reported to account for up to 2 % of the initial thickness and the overall expansion was up to 4 % of the initial thickness of the cell.

Rieger et al. [82] investigated the expansion of 2.3 Ah LCO/G cells with two opposing contact displacement sensors, each located at the center of the cell. The measurements made are compared with the mean values of a 3D structured light camera system. Rieger et al. concluded that 1D-dilatometry can be used to calculate the SoC-dependent electrode swelling for electrochemically and mechanically coupled models for battery cells.

Louli et al. [99] used a 1D-dilatometer setup to investigate the volume change of NCA/SiO-G cell with a capacity of 260 mAh. The cathode material had x and y values of the single components between $0.05 < x < 0.15$ and $0.02 < y < 0.10$. A single stacked battery cell consisting of only one positive and one negative electrode was built for this measurement. The displacement sensor was located in the middle of the cell. A spring was installed to exclude local expansion due to gas formation. The applied pressure was limited to 30 kPa, which has no impact on the cell behavior. The result, shown in Figure 4 (**b**), showing an asymmetric behavior for charge and discharge. This asymmetry is a sign of hysteresis between the charge and discharge cycles. It is also shown, that the thickness change is not linear with the SoC for this battery cell.

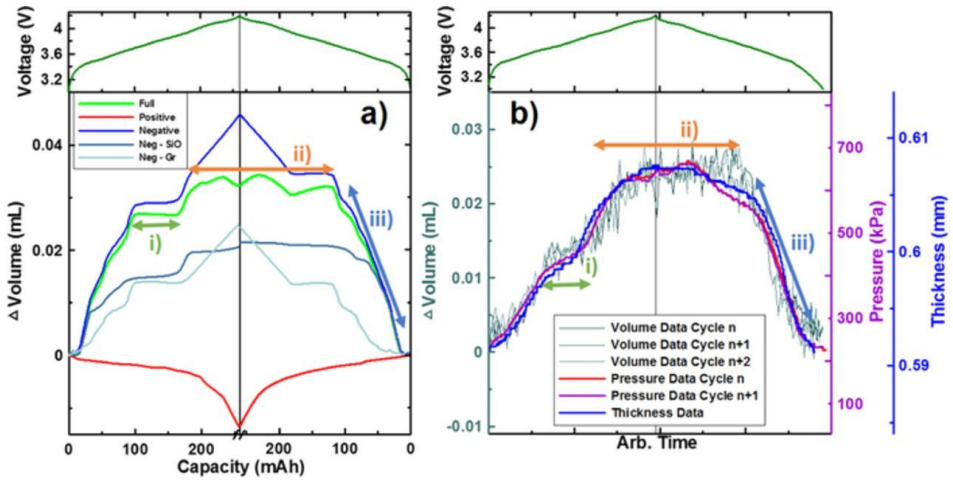

Figure 4. Calculated volume change of each electrode at charge and discharge cycle (**a**). Results of measured volume, pressure and thickness change for NCA/SiG cell; Reproduced under Creative Commons License without any changes (CC BY 4.0 by Louli et al.[99])

Vorwerk et al. [52] used 1D-dilatometry measurements to log the cell expansion during abuse testing. They performed tests under critical cell conditions with overcharging, reaching a SoC over 100 %. The investigated cells were NMC/G cells with a capacity of 75 Ah. The measurement setup was similar to the one shown in Figure 3 (b). It was discovered that there was a significant increase in cell expansion at a SoC of 112 % up to

2.2 mm (17 % of initial cell thickness). This expansion could be explained by gas production due to decomposition reactions of the active material. After the cycle was stopped, the cell was allowed to relax for 45 h to ensure that no cell bursting or fire occurred. In this time, the expansion increased by further 5 %. As a result, they concluded that the expansion of the cell starts far ahead of events like cell bursting. Expansion of battery cells could be an indicator for monitoring the safety of battery cells.

Berckmans et al. [100] investigated the influence of external pressure on battery cells with two different chemistry types. One cell is constructed with a NMC532 cathode, and the other with a NMC622 cathode. The anode material was a silicon-graphite alloy. The measurement apparatus used is similar to the one demonstrated in Figure 3 (**b**). The dial gauge was replaced with a force sensor between the top mounted plate and the pressure plate on top of the battery cell. In this study, the force exerted due to the cell expansion is measured, instead of the expansion itself. Figure 5 shows the voltage and current in the top graph from the OCV test, whereas the lower graph shows the exerted force. The force could be divided into three main stages. The first red stage shows nearly constant behavior, which could be explained by the quantity of graphite in the anode alloy, which experiences less volume expansion than silicon during intercalation [101]. Delithiation in graphite occurs at potentials of 0.1-0.2 V vs. Li/Li^+, whereas in silicon deintercalates at potentials of 0.3-0.5 V vs. Li/Li^+ [27,102–104]. This is one possible reason for constant force readings at the beginning. Further tests demonstrated that there is no C-rate dependency on the induced force due to intercalation.

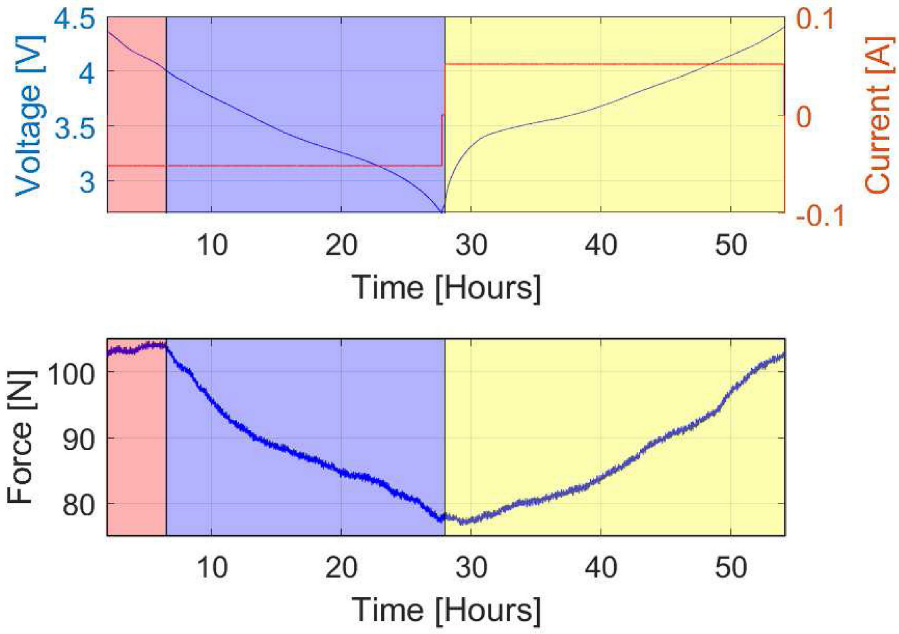

Figure 5. Quasi-open circuit test: Voltage, current and caused force variation on NMC/Si-G pouch cell at 25 °C; Reproduced under Creative Commons License without any changes (CC BY-NC-ND 4.0 by Berckmans et al. [100])

Jin et al. [105] performed tests to evaluate the stress from battery cells cycled under constant thickness and the thickness evolution of battery cells under constant force. For the stress measurement, a similar setup to Berckmans et al. [100] was used. The thickness measurement was performed with constant load applied to the top of the cell, and was made with a high-speed camera. A NMC532/G cell with a nominal capacity of 1.6 Ah was chosen for these measurements. The applied stresses were 34.5 kPa and 172.4 kPa. For the thickness measurement the applied stress was 103.4 kPa, as determined from previous experiments. The cells were charged at different C-rates and upper cut-off voltages. As a result, for the stress measurement, it was concluded that the stress increased with a higher

upper cut-off voltage, but decreased if the initial stress or the C-rate are increased. The thickness on the other hand increases if the C-rate of the upper cut-off voltage are increased, but the thickness evolution is decreased if the initial stress is increased.

Louli et al. [99] investigated both 1D-dilatometer measurements and the force exerted by an NCA cell. Two additional chemistries were also investigated: LCO/Si and NCA/nano SiC with capacities of 230 mAh and 165 mAh respectively. The NCA cathode material had x and y values of the single components between $0.05 < x < 0.15$ and $0.02 < y < 0.10$. For this measurement a setup with two enclosure walls was used, in which a defined pressure through a screw with one adjustable enclosure wall can be generated. Between this casing, the pouch cell is placed with a pressure plate and the pressure sensor. The cells were cycled for more than 1,000 h at 40 °C and charged with a C-rate of C/3. An irreversible increase in pressure was observed over the time. The LCO/SiG-alloy battery cell had a much higher irreversible volume expansion. The reversible pressure for two different cycles is shown in Figure 8 (**b**) in orange and violet. The pressure measured has a similar asymmetric behavior as the measurement with the 1D-displacement sensor mentioned earlier.

Stock et al. [95] used a setup to measure the gas production and the swelling of the cell with a 1D-dilatometer. An adjustable pressure plate was fixed by four springs onto the surface of the cell with a pressure of 200 kPa. A tactile displacement sensor was located at the center of the plate to measure the swelling behavior of the cell. A second plate was placed on the gas bag which was attached to the cell without any extra pressure applied. This plate is free to move in one direction and a second tactile sensor is placed in the center of the cell. Through the applied pressure on the cell, the gas is forced to move into the attached gas bag. Through calibration, the accuracy of the volume measurement is 0.6 µl. The authors showed that the main gas production and the expansion in acnmc622/G cells and NCA/SiC cells occur during the formation cycles. Another result was that the gas production with respect to the cell voltage in NMC/G cells diminishes when the dilation begins to increase. This is explained by the fact that the formation of the SEI layer begins before the lithiation of the graphite anode.

Bitzer and Gruhle [69] used 1D-dilatometry to detect lithium plating *in-operando* in NMC pouch cells. The state of the art to detect lithium plating was to measure the negative anode potential vs. Li/Li^+ with a reference electrode or in a half cell configuration. Initially, they started with calculating the molar masses of the transferred charge. They found that plating should lead to an increase in volume expansion, since the intercalation of lithium ions in graphite results in a lower expansion than the deposition of metallic lithium on the anode surface. Figure 6 shows the expansion behavior of the transferred charge with and without plating measured with the 1D-dilatometer. It could be seen, that the absolute expansion with high current (red) is much higher than with a low current (blue). The peak arises at the constant voltage phase and decreases when the charge is stopped. Through decomposition of electrolyte, gas is produced. The presence of gas can introduce errors on the measurement of the expansion of electrodes. In order to differentiate the swelling of the pouch cell caused through gas production or electrode expansion. Bitzer and Gruhle [69] proposed a method including a spring directly coupled to the dial gauge. The spring adds a defined force against the battery cell and any gas will move sideways and only solid expansion will add enough force to contract the spring.

Grimsmann et al. [106] performed 1D-expansion measurements with a setup similar to the one in Figure 3 (**b**). They compared the expansion of calendaric and cycle aged cells, as well as cells with provoked lithium plating. To induce lithium plating, 22 Ah NMC cells were placed in a climate chamber at 0 °C and were charged with high currents. As a result, they confirmed and expanded on the findings of Bitzer and Gruhle [69]. The expansion of the cells with lithium plating is higher than the expansion from cycle aging under normal condition. There is also a difference in the expansion behavior based on the dominant degradation mechanism in the cell. The three tested mechanisms showed different swelling behavior.

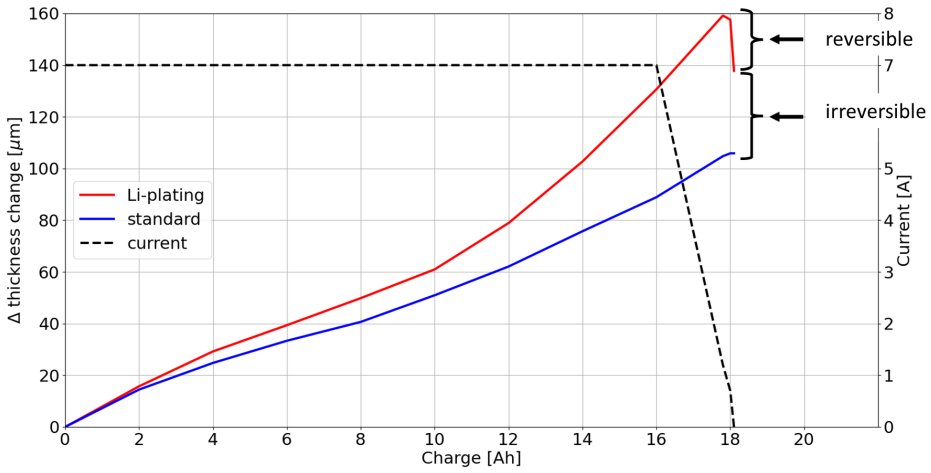

Figure 6. Expansion behavior of a pouch cell with and without lithium plating while charging (own representation based on data from [69])

Oh et al. [107] studied the expansion of a 5 Ah prismatic NMC/G cell. Five contact displacement sensors were mounted on the surface of the cell. One was placed at the center of the surface and the other four were located in a cross pattern on the top, the bottom, left and right of the center probe. On the opposing side, one extra displacement sensor was located on the center of the surface. They came to the conclusion that the greatest expansion takes place in the center of the cell with 1.5 % expansion with respect to the initial thickness and around 0.75 % for the other positions. The measured expansion on the left and right side was smaller than on the upper and lower sensor. Also, the expansion decreases towards the edges with a maximum expansion of 0.55 % on the right and left side and around 0.3 % for the top and bottom. This difference could be caused by the mechanical constraints of the cell housing. The variation of the ratio between the center and the other locations are similar. Therefore it was concluded that one sensor in the center can accurately quantify the cell swelling.

3.1.2. Buoyancy Measurements

Aiken et al. [108] were the first to use the Archimedes principle to measure the amount of produced gas in the formation cycling of battery cells. The purpose of this measurement was to understand the behavior of gas production during formation cycling and in undefined conditions, such as electrode / electrolyte redox reactions. They made use of an apparatus resembling the the left image in Figure 7. They immersed a cell in a non-conductive fluid and hung it from a balance on the top of the apparatus. By placing the cell into liquid, a buoyant force F_b acts on the cell.

$$F_b = \rho_{Fluid} \cdot g \cdot V_{Cell} \tag{1}$$

where ρ_{Fluid} describes the mass density of the fluid, g defines the acceleration due to gravity and V_{Cell} is the volume of the cell. In Figure 7, the right side displays the active forces acting on the cell. In stationary conditions, the balance of forces is, according to Ref [95], as follows:

$$F_g = F_b + F_t + F_{w,||} \tag{2}$$

where F_g is the measured force, F_t is the tension force by the hook and $F_{w,||}$ is the force due to the connection wires. Since the measured force and the wire force remain constant due to the same mass, changes in the measured force are only a function of the volume of

the cell. This leads to changes in the buoyant force and therefore in the tension force. F_t can be represented as:

$$\Delta F_t = \Delta m_{balance} \cdot g = -\rho_{Fluid} \cdot g \cdot \Delta V_{Cell} = -\Delta F_b \tag{3}$$

Rearranging equation 3 according to the change in volume gives:

$$\Delta V_{Cell} = -\frac{\Delta m_{balance}}{\rho_{Fluid}} \tag{4}$$

With this equation, the volume change of the cell can be derived from the mass measurement registered on the balance.

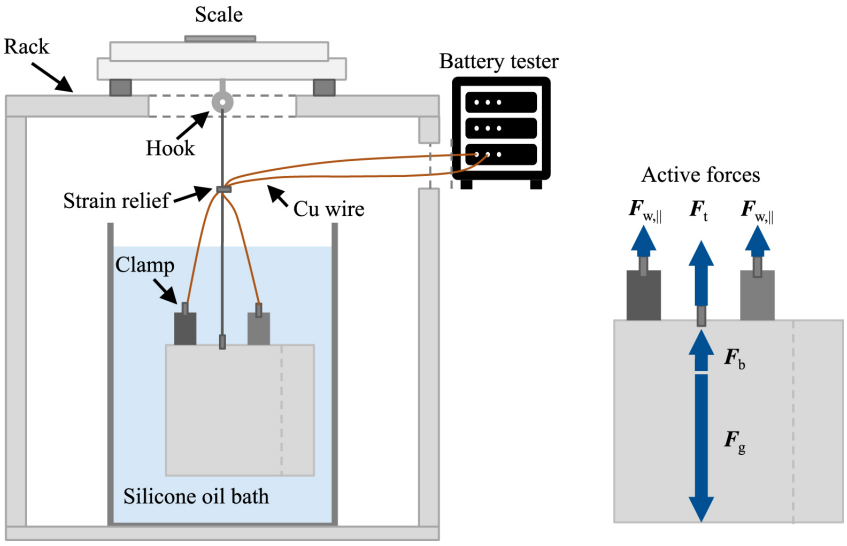

Figure 7. Setup for Immersion Bath Measurement: Evaluating the volume expansion in battery cells due to gas evolution and electrode dilation, along with active force display. A pouch cell is affixed to a high-precision balance via a 0.5mm diameter copper wire and linked to a battery tester through thin, insulated copper wires. Strain relief is applied to the cables to guarantee that the total weight is supported by the scale. The cell is completely submerged in a non-conductive liquid bath within a controlled climate chamber. The accompanying diagram illustrates the active forces exerted on the cell; Reproduced under Creative Commons License without any changes (CC BY 4.0 by Stock et al. [95])

Aiken et al. [108] investigated gas formation with different kinds of electrolyte with the apparatus shown in Figure 7. They used NMC111/G cells with a capacity of 225 mAh. Nine cells were investigated. Five cells were clamped between pressure plates to ensure a constant force on the cells surface, and the remaining four cells were cycled unconstrained. During formation, the immersion bath was placed inside a climate chamber and heated up to 40 °C. In the first cycle, the clamped cells produced a large amount of gas in a short time and then remained constant. The unrestrained cells, on the other hand, form an initially higher quantity of gas, which then decreases very quickly. This is explained by the fact that the gas is diverted into the gas pocket in the clamped condition and has little time to react with the electrodes. In a second test, formation cycles with different currents were performed. They concluded that during the formation cycle, the composition and the quantity of the gas produced is similar, as long as currents remain below C/3.

Stock et al. [95] used both the Archimedes principle, and 1D-dilatometry to compare the gas production of two different cells in the formation cycle. One cell had a NCA cathode with a SiC anode and the other had a NMC cathode and a graphite anode. Similar to the Aiken study, the authors investigated gas formation in both compressed and uncompressed cells. Measurements on the compressed cells were made using 1D-dilatometry with a pressure plate on the cell surface to apply pressure. Measurements on uncompressed cells

where made using the Archimedes principle, as was done in the Aiken study. Figure 8 shows the expansion measured for both measurement techniques with the NCA/SiC cell on the left-hand side and the NMC/G cell on the right-hand side. For the NCA cell, both measurements provide similar results, for the NMC, however, the two measurements provide different results. This is explained by the fact that the unstressed cell initially produces a large amount of gas in the liquid phase of the graphite intercalation, which later reacts to form liquid or solid components in the graphite structure. In the tensioned structure, no reduction reaction can take place due to the applied pressure. Cell dilation is described as the main expansion influence.

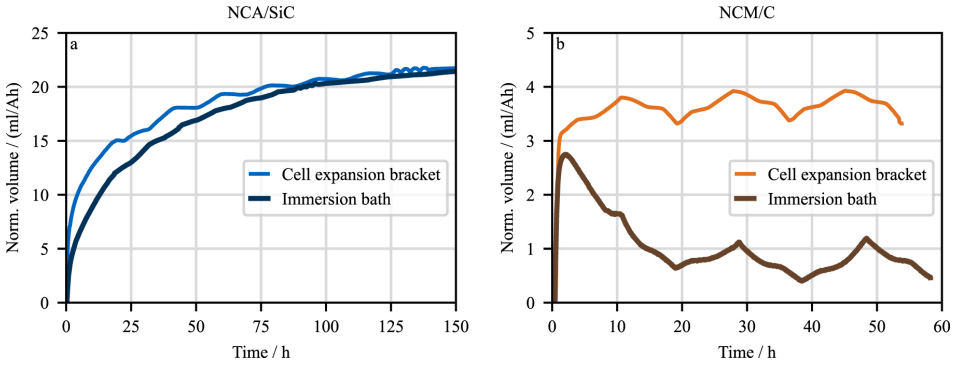

Figure 8. Comparison between 1D-dilatation measuring of gas production through pressure plate and immersion bath. Normalized volume for NCA/SiC cells (**a**). Normalized volume for NMC/G cells (**b**); Reproduced under Creative Commons License without any changes (CC BY 4.0 by Stock et al. [95])

Leißing et al. [109] investigated the influence of the C-rate on the gassing behavior of NMC622/graphite cells with nominal capacity of 5 Ah. To determine the amount of gas which is produced on formation cycles, the same apparatus as Aiken et al. is used [108]. They charged the cells at different C-rates and measured the volume differences due to gas production directly after reaching the lower cutoff voltage. The most gas is produced (7.7 ml) with a C-rate of 2C and the least amount of gas (1.6 ml) is produced with a C-rate of 0.1C. The lowest C-rate of 0.05C produces, in contrast, a comparatively high amount of gas (4.2 ml). This is explained due to the long time spent at lower potentials. The extended formation time leads to an increase of electrolyte reduction and more parasitic reactions.

Louli et al. [99] used the principle of buoyancy force, in addition to pressure measurements and the 1D dilatometry measurement to measure the volume change of battery cells during charge and discharge cycles after formation. They compared all three measurement techniques, shown in Figure 4. All three techniques demonstrated similar behavior in volume expansion, leading to the conclusion that all techniques are suitable for this type of measurement.

Many of the proposed methods for applying Archimedes' principle use the technique to measure gas evolution in battery cells during the formation cycles with different electrolyte compositions [110–116] or with electrodes with different chemical compositions [117].

3.1.3. Strain measurement

To establish reliable condition monitoring for lithium-ion batteries, it is advantageous to integrate strain measurement into the classical electrical measurements of battery cells [118]. The expansion of the cell induces deformation in the housing due to strain. In their study, Hickey and Jahns [119] demonstrated a correlation between cell expansion and the strain on the cell's housing. The strain imposed on the cell's housing by internal expansion mechanisms can be quantified using either strain gauges or optical solutions such as fiber braggs grating (FBG) sensors.

Strain gauges

Strain gauges convert distortions from stress and strain into electrical resistance, which can be measured. Hickey and Jahns [119] combined measurements with strain gauges and tactile displacement sensors to assess the feasibility of SoC estimation. For this purpose 5.5 Ah prismatic cells were cycled. Three strain gauges were placed, with two gauges on the opposing side near the center of the cell and the third gauge near the exhaust vent. The tactile sensor served as a reference placed at the center of the cell. Figure 9 shows strain measurements at the vent position on prismatic cells are comparable with the 1D-displacement measurements during a discharge pulse measurement with a current of 0.5 C. Moreover, SoC estimation of the battery cells is possible with this apparatus.

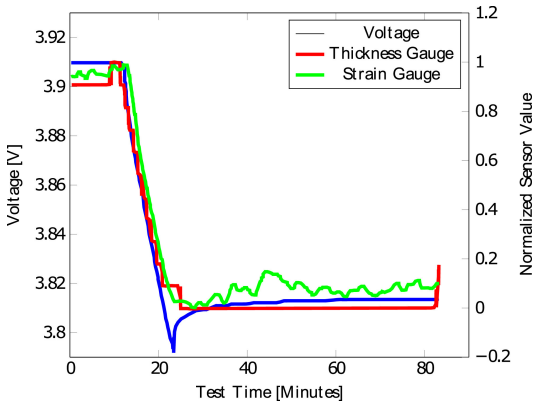

Figure 9. Response of the cell voltage, the cell expansion (1D-dilatometer or thickness gauge) and the strain of the cell surface (strain gauge) to a 0.5 C discharge pulse of a prismatic cell; Reproduced under Creative Commons License without any changes (CC BY 4.0 by Popp et al. [42] with Data from [119])

Choi et al. [120] performed tests under abuse conditions using carbon nanotube (CNT)-based strain sensors to measure the volume change of a pouch bag caused by excessive temperature fluctuations. For this purpose a cell is heated to approximately 90 °C until gas leakage occurs due to excessive gas production. The complete deformation of the cell with good time resolution is measured, leading to the conclusion that this setup could be used for real-time measurements.

Willenberg et al. [121] investigated the correlation of the overall impact of the cell expansion on the cell ageing. They cycled 51 commercially available 18650 cylindrical cells with an NCA cathode and an anode made of graphite and a small amount of silicon. The nominal capacity of the cell is 3,350 mAh. The cell had an initial diameter of 18.55 mm and is wound 19 times in the housing. The cell was aged with at 0.5 C with a average SoC of 50 % and a cycle depth of 50 %. They found, that there is a discrepancy in the diameter change between the charge and the discharge cycles. The authors explained this behavior as being caused by the different intercalation stages of lithium ions during charge and discharge. For the 51 cycled cells, they found an average diameter change of the cells of 10.7 µm with a standard deviation of 4.4 µm. Up until the cell diminished to a state of health (SoH) of 80 %, there was a slight increase in the irreversible diameter change. In contrast, a large increase in the irreversible change occurred when the cell approached a SoH of 60 %. After 700 cycles, they found a significant increase in the cell diameter, as well as in the temperature of the cell. Postmortem analyses showed the irreversible diameter change in form of a deformation of the inner windings. The authors concluded that there was a correlation between the capacity fade of the battery cell and the change of the battery cell diameter. They also showed that it is possible to measure both the reversible and irreversible volume change in cylindrical battery cells using strain gauges.

Optical fiber sensors

Fiber Braggs Grating (FBG) have been established as a standard fiber optic sensor for monitoring battery conditions. Typically employed for measuring *in situ* strain and temperature, this sensor type is based on an optical fiber with a grating featuring a defined period [122]. The grating is inscribed into the optical fiber core by the interference of two coherent ultaviolet (UV) light beams [123].

Figure 10 (**a**) shows the unloaded FBG sensor on the left side. A broadband light source is used to send a certain light intensity I_I through the optical fiber. The grating then acts as a filter and reflects a light intensity I_B with a pre-defined wavelength, referred to as the Bragg wavelength. The remaining light intensity I_T, composed of the unfiltered wavelengths, is transmitted and monitored using an optical sensor. The Bragg wavelength can be represented as

$$\lambda_B = 2n_{eff}\Lambda \tag{5}$$

with λ_B as the Bragg wavelength, n_{eff} as the effective refractive index of the grating and Λ as the period of the grating [124] . The Bragg wavelength can be influenced by external effects such as strain or temperature [125]. In the case of an applied strain on the optical fiber, the period of the grating λ_{UV} changes. As a result, the reflected Bragg wavelength changes as well. The wavelength increases for tensile forces and decreases for pressure forces applied on the length of the fiber, as shown in Figure 10 (**b**). The resulting wavelength shift can be described as

$$\frac{\Delta\lambda_B}{\lambda_B} = (1 - p_e) \cdot \varepsilon \tag{6}$$

with p_e as the photoelastic coefficient and ε as the strain $\Delta l / l_0$ [126].

A secondary influence on the reflected wavelength is the external temperature, as shown in Figure 10 (**c**). A change in the temperature results in a change in the effective refractive index n_{eff} [127]. The change due to thermal influences is effectively a superposition of a change of the refractive index and thermal expansion. The shift in refractive index has a dominant effect and accounts for up to 95 % of the expansion, with thermal expansion playing a minor role [128].

FBG sensors are immune to electromagnetic interference, chemically inert, mechanically robust and the use of multiple sensors is possible [122,125]. Many of the proposed methods, including optical fiber sensors, were developed to measure the temperature of the battery cell and not the strain induced due to reversible and irreversible expansion [122,129–132]. Since the main focus of this review is the expansion behavior of lithium-ion battery cells, the strain measurement of optical fiber sensors is of greater relevance.

Yang et al. [133] were the first who had applied FBG sensors onto the surface of battery cells. Their aim was to monitor the external temperature of the battery cell surface. For this purpose, seven Bragg sensors on one string were installed and coupled to the top and the bottom of three cells. The seventh sensor is installed in the climate chamber to measure the ambient temperature. They were able to measure the temperature under different charging conditions. Compared to thermocouples, this sensor was also able to response to dynamic inputs.

Sommer et al. [134] extended the measurements beyond temperature monitoring, to the characterization of intercalation stages of lithium-ion batteries during charging and discharging cycles. For this purpose, they installed two FBG sensors on the top of a 15 Ah NMC/G pouch cell. They used a temperature compensation method based on a reference FBG sensor proposed by Rao [135]. This method makes use of one FBG sensor bonded directly to the surface of the cell to measure both thermal and strain effects, and a second FBG sensor that is loosely attached to measure only thermal influences. The measurement from the second sensor are subtracted from the first, to isolate for strain. The cell was then clamped between two pressure plates with foam on either side to allow the breathing of the cell. The breathing of the cell refers to the reversible expansion

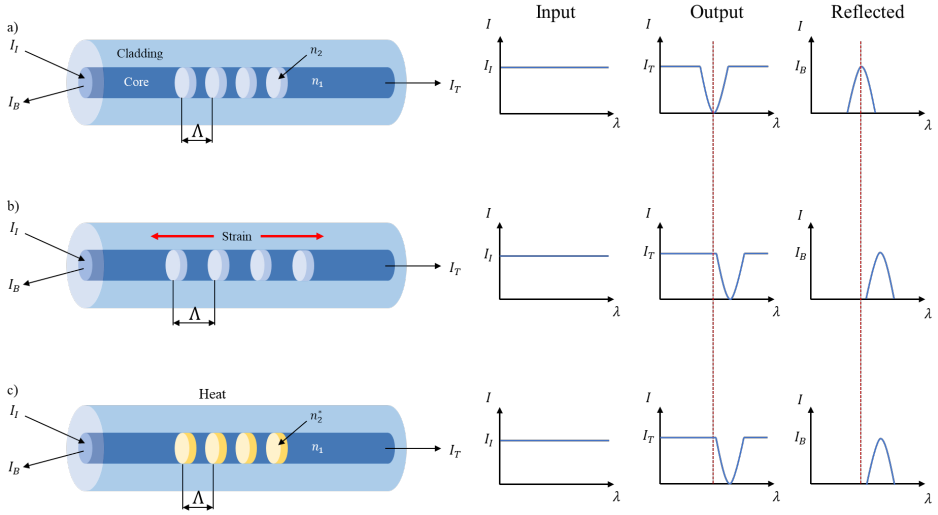

Figure 10. Functionality of a FBG sensor. Shown are the physical changes due to heating and strain with respect to the input, output and reflected light spectrum. With no external strain and ambient temperature FBG sensors have specific inputs, outputs and reflected profiles (**a**); If there is a external stress applied on the FBG, the same input will have a different output and reflected profile due to a shift in the grating profile. The direction of the stress, such as tensile and compressive force, will define the increase or decrease of the reflected wavelength (**b**); Due to external heating or cooling of an FBG sensor, the effective refractive index n_2^* will change. This will lead to a increase or decrease of the reflected wavelength (**c**); Own representation based on Wahl et al. [122] under Creative Commons License (CC BY 4.0)

occurring during charge and discharge cycles. Using these measurements, a correlation was established between the derivative of the SoC and the shift of wavelengths with respect to the measured voltage, during cycling under normal conditions. The authors concluded that the shift of wavelengths, which define the strain on the surface of the cell due to cell expansion, can indicate the different intercalation stages for charging and discharging. In a second publication [136], they monitored the relaxation behavior of the same cell with the same sensor configuration but without the pressure plate. They demonstrated that it is possible to measure the ion diffusion of lithium-ions intercalating into the graphite host lattice. For higher temperature values at higher SoCs, the wavelength shift is less than at lower temperatures. In these experiments the wavelength shift began to differ for SoC levels of approximately 65 %. They concluded that the ion diffusion in the host lattice is a thermodynamic process and the higher temperature helps to overcome the van der Waals gap between two adjacent graphite layers. After a longer period of rest, the ions are distributed homogeneously in the lattice and consequently the wavelength shift decreases.

Meyer et al. [137] observed the strain behavior, and consequently, the volume change of a battery cell with two FBG sensors. One sensor was directly attached to the surface to measure external strain and thermal effects on the cell surface, while a second sensor, housed in a heat-conductive protection tube, was installed on the cell's surface to specifically measure external thermal influences. Measurements were made on a 40 Ah NMC/G battery cell and was cycled under normal and accelerated aging conditions. To accelerate the aging of the cell, tests were performed under increased temperature conditions. The normal condition tests were not heat compensated and showed the superposition of both the external strain and thermal influences. In the accelerated aging tests, the thermal influences were compensated, and a correlation between the relative capacity loss over 400 cycles and increases in the strain difference was present.

Raghavan et al. [138] investigated a solution to embed FBG sensors inside a pouch cell and seal the pouch bag around this sensor. The sensors were placed in the middle of the cell area in the middle of the electrode stack. To measure strain and temperature, one sensor

was located in a thermally-conductive housing tube and one was directly attached directly on the separator. The number of cycles to reach the end-of-life for the cell with embedded FBG sensors was approximately 200 cycles less than for an equivalent cell without the embedded sensors. Regardless, the cell reached a cycle life of more than 1,100 cycles. They concluded that estimations of SoC and SoH made with information from the embedded sensors are more accurate than predictions made without.

Bae et al. [139] extended the strain monitoring of battery cells by embedding the FBG sensor directly into the graphite structure of the negative electrode. They compared this solution with a configuration where the sensor was attached between the graphite and separator layer on the negative electrode. Electrochemical performance tests confirmed that there is no significant influence of the implanted sensor on the performance of the electrode. Figure 11 compares the wavelength shift for a charging cycle for both the attached sensor (left) and the implanted sensor (right). The shift occurs with increasing SoC towards longer wavelengths. In the implanted approach the shift is observed, in addition to a split in the observed wavelengths. This is explained as the superposition of two different applied stresses on the sensor. The attached sensor is only influenced by the longitudinal stress in the direction of the fiber. The transversal stress is, in this case, relieved by the flexible separator foil. In contrast, the implanted sensor is influenced by the longitudinal stress as well as by the transverse stress, due to its location in the more rigid structure of the graphite. Since the sensor diameter is on the same order of magnitude as the thickness of the negative electrode, the authors suggest that the results are qualitative.

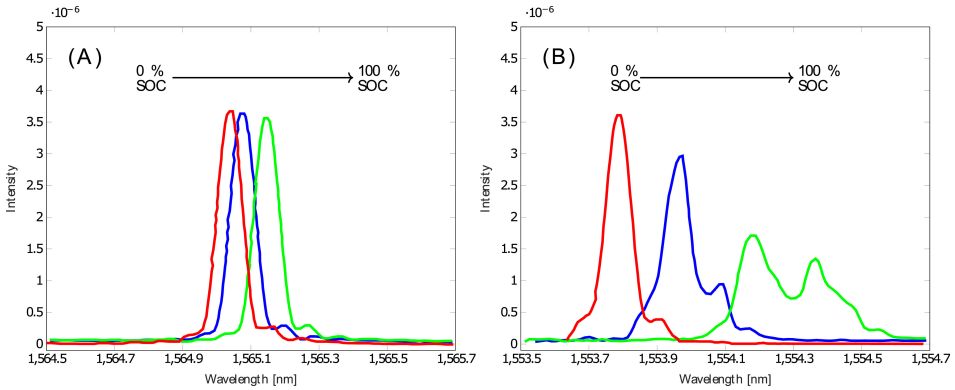

Figure 11. Wavelength shift over SOC for attached FBG sensor on graphite anode (left) and implanted sensor (right). Each spectrum shows different SoC stages: 0 % = red, 50 % = blue, 100 % = green; Reproduced under Creative Commons License without any changes (CC BY 4.0 by Popp et al. [42] with Data from [139]

Nascimento et al. [140] extended the FBG sensor with a fabry-perot (FP) cavity sensor. FP cavity sensors are typically used for strain or pressure measurements. This sensor is robust against temperature shifts. It is designed with two parallel reflecting surfaces and the phase of the reflective wavelength is measured. Any shift in the phase can give insights on the applied longitudinal strain or pressure. If the FBG sensor is located near the FP sensor, it is possible to measure temperature and strain with a single hybrid sensor. To test this sensor, the authors placed three sensors close to the tabs of the cell, in the center of the cell and on opposing side of the tabs. The sensors are located between two separator layers inside the cell. It is then possible to measure internal strain and temperature. Single FBG sensors were placed on the surface of the cell in same location as the hybrid-sensors to compare the temperature results. The hybrid sensors show a slightly higher temperature increase than the a single sensor mounted on the surface. The authors concluded that with this hybrid sensor it is possible to monitor the internal temperature and strain in battery cells.

Most of these solutions focus on extended safety measurements for battery management systems (BMSs) in automotive applications [134,136–138,141–144]. The objective of

these measurements is to improve SoC and SoH estimations, increasing safety in dynamic-use applications, like EVs. Future efforts are leveraging machine learning (ML) and artificial intelligence (AI) to gain better insights from FBG sensor measurements in the estimation of critical conditions [145].

3.2. Non-contact approaches

In many use cases, it is preferable to make use of a non-contact approach to measure volume expansion on battery cells. Non-contact approaches have the advantage of not influencing the expansion of the cell by inducing local pressure spots, where local degradation might be induced and error in the measurements introduced. In addition to having effectively no wear on the sensor due to the lack of contact. These approaches can be mainly divided into radiological and optical measurement techniques.

3.2.1. Radiological imaging

Radiological measurements can make use of either x-ray or neutron beams. By using this technique the inner components of the battery cells can be visualized in microscopical level without damaging it. Radiological imaging can be performed *ex situ*, where the part to be imaged is extracted from the battery, or *in situ*, where the imaging is performed on the entire cell, and *in operando*, with the imaging being performed during cycling [146].

X-ray imaging

X-ray imaging is widely used to characterize lithium-ion battery components. The investigation can vary from individual electrodes to defects in the cell casings. The x-ray beam is generated by either electrons accelerated in a x-ray tube, or by a synchrotron particle accelerator. Synchrotrons are capable of providing much greater acceleration than an x-ray tube, resulting in orders of magnitude greater brilliance in the x-ray beam [147]. The higher brilliance beam enables greater material penetration, the imaging of smaller features, and much faster imaging than it is possible with beams generated by an x-ray tube [148]. Naturally, these advantage come at an extremely high cost, requiring a dedicated facility, rather than a lab-compatible x-ray tube apparatus [148,149].

In situ or *in operando* measurements are generally more desirable, as neither require the disassembly of the cell. However, the measurement quality of the interior of the cell is often poor due to the attenuation of the x-ray radiation by the metallic battery casing [150]. To reduce x-ray attenuation, some researchers design special battery casings [151–153]. These solutions introduce an x-ray penetrable window, often made of materials like kapton or thin metal films, to minimize attenuation from the case in the resulting x-ray image. The cell casing ultimately exists to ensure good mechanical and electrical contact between the battery components, such as electrodes and electrolytes, and to keep the cell free from oxygen and moisture. By introducing a special window, it is possible that the permeability increases for long term cycling, or that the mechanical properties will be compromised. As a result, the expansion behaviour and cell performance might be affected, meaning results may not be entirely similar to those from conventional commercial cells. Even with the special casings, it is often necessary to use synchrotron generated beams to achieve the required contrast in imaging [151,153].

Bond et al. [154] made use of synchrotron radiation to evaluate geometry changes *in situ* in the electrodes after over-discharging a pouch cell to induce gas formation. A 200 mAh LCO/G pouch cell was imaged first at 50 % SoC, and then was discharged to −500 mV, with initial swelling becoming apparent as the cell reached a potential of 0 V. After holding the cell in over-discharge, computed tomography (CT)-imaging was performed using a synchrotron beam line with an energy range of 30 keV to 40 keV. Given an x-ray beam size of 2 mm, Bond et al. performed multiple measurements and then stitched the resulting images together, resulting in a total imaging time of about 30 min. This study revealed greater separation between electrodes in the center of the battery cell. A total 6.3 % expansion was observed in the axis perpendicular to the flat sections of the jelly

roll, with electrode layers closer to the outside contributing the most to the cell expansion. Even with high-energy x-rays from a synchrotron, the graphite electrode is difficult to differentiate from other components, because it is a light element. The cathode can be visualized, as it is composed of relatively heavier elements [154].

Pietsch et al. [146] demonstrate *in operando* simultaneous x-ray diffraction and x-ray tomographic microscopy on an experimental lithium-ion half-cell using a synchrotron beam. The half-cell is composed of a silicon powder electrode, a glass fibre separator, and a metallic lithium electrode, contained within a thermoplastic casing. Silicon was selected as the anode due to its high degree of volume expansion, and academic relevance. Silicon electrodes have shown volumetric expansion during cycling of up to 280 % of its initial volume [155,156]. Not only were Pietsch et al. able to demonstrate the volume change in both the anode and cathode during cycling, but also the structural change in the silicon electrode. The transitions from pure silicon to a lithium-silicon alloy in the silicon anode during lithiation can be observed through x-ray diffraction [157]. This experiment required a 42 keV beam. A tomographic scan requires 20 min, and x-ray diffraction 1 min. For each image type 48 scans were taken.

In cases where x-ray imaging is used to characterize changes in the casing of battery cells, lower intensity x-rays can be applied [158]. Wang et. al performed *in situ* imaging using an x-ray tube based system. The x-ray beam intensity was not sufficient to penetrate through the whole battery cell, therefore, only distortions in the pouch cell casing were detected. When x-rays with low intensity were used to image the casing, the images obtained were similar to those that can be taken with a standard optical camera.

Due to the attenuation of x-rays through the metallic casing and separator foils, it may be preferable to take an *ex situ* approach to obtain high contrast electrode images [159,160]. The disadvantage of using an *ex situ* approach is that the cell must be disassembled. The disassembly of the cell must be done in an environment with low moisture content, like a glove box, to prevent uncontrolled chemical reactions on the electrode. .

Finegan et. al [159] performed both *in operando* CT measurements using a synchrotron x-ray source during overcharge abuse testing of a LCO pouch cell, and afterwards *ex situ* x-ray CT measurements as a part of post-mortem analysis. The authors were able to observe from the *ex situ* measurements evidence of cobalt deposition on the cathode. However, the majority of the cell expansion could be attributed to gas formation, as observed in the *in operando* measurements.

Neutron imaging

In contrast to x-ray, neutron imaging offers good transmission through heavy elements, and lower transmission through light elements. This means that neutron imaging has a better ability to "see" through the metallic battery casing [161]. Siegal et al. applied neutron imaging to detect changes in the anode and cathode layers during charge and discharge cycles. In addition to yielding information about the deformation of the electrodes, Siegal was also able to observe the *in operando* movements of lithium ions during cycling. Unlike x-rays, which are blocked by heavier elements, neutron beams have low transmission through lighter elements, such as lithium. When high concentrations of lithium ions are present, lower neutron counts are detected. This is particularly useful for identifying the location of lithium ions at various states of charge [162]. For example, when the battery cell is in a charged state, due to intercalation of lithium ions, there will be fewer neutrons detected at the anode [5]. Though neutron imaging is advantageous for *in situ* imaging, it requires fission reactions from a nuclear reactor. This makes the imaging technique expensive and generally inaccessible in nearly all commercial and in many academic environments [163].

3.2.2. Optical Imaging

Optical approaches offer the advantage of being more easily deployable than radiological techniques. Optical approaches are generally limited to measuring changes at

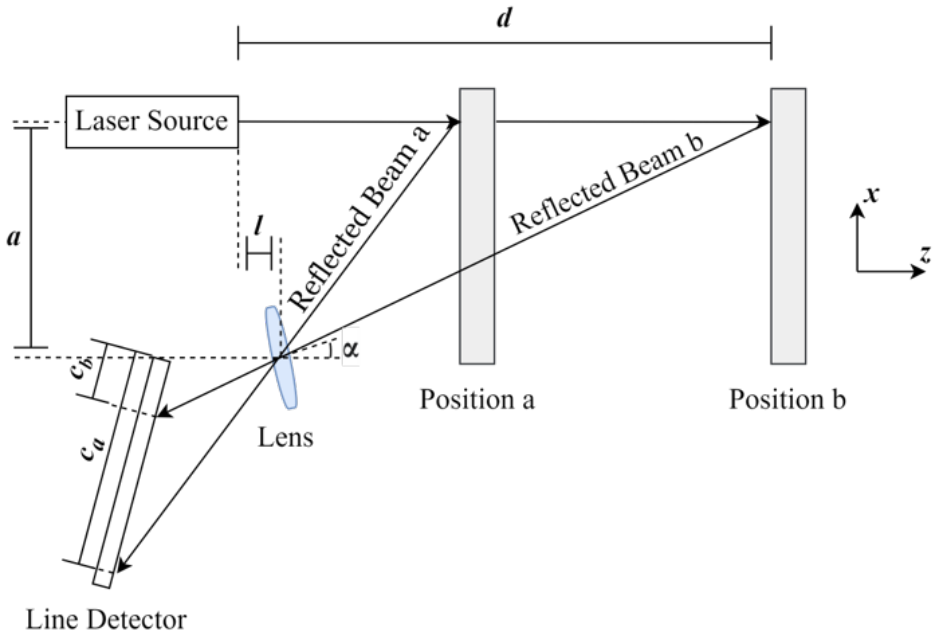

Figure 12. Basic apparatus for laser triangulation for objects with a diffuse surface [166,168,169]

external surfaces. In the literature, researchers typically make use of one of three imaging technologies: laser triangulation, interferometry, or camera-based 3D-imaging techniques.

Laser Triangulation

Laser triangulation has been used to create 1D and 3D-profiles of the expansion of lithium-ion cells during cycling [164,165]. Due to the small imaging spot, a high spatial resolution is achievable. In addition, modern laser triangulation sensors offer positional measurements with high accuracy. However, like most measurement techniques, there is a trade off between field-of-view and resolution. In the case of 1D-imaging, high sampling rates are possible, as the only limitation in acquisition speed is the exposure time of the camera. Laser triangulation makes use of a relatively simple measurement principle, where only a source laser, a lens, and a line detector as shown in Figure 12 are required. [166,167]

In an ideal system, the position c_d, measured on the line detector, will solely be a non-linear function of the distance d, given by the following equation

$$d = \frac{f}{\cos\alpha}\left(1 + \frac{\sqrt{a^2 + \left(a\tan\alpha - \frac{f}{\cos\alpha}\right)^2}}{c_d}\right) - a\tan\alpha - l \tag{7}$$

where f is the focal length of the lens, α is the angle between the z-axis and the centerline of the lens, a is the vertical distance between the incident beam propagation axis and the center of the lens, and l is the horizontal distance between the laser and the center of the lens as demonstrated in Figure 12 [168].

Laser triangulation sensors require a non-negligible footprint due to the offset between the lens and the laser source. This offset is ultimately determined by the desired measurement range. Though it is possible to use equation 7 to map c_d to d, calibration procedures are typically used instead to handle the influence of optical aberrations and mechanical tolerances [169]. Even micron-scale mechanical instabilities and thermal gradients can lead to shifts in the measurement, beyond the scope of the calibrations [166]. To a certain extent, these issues can be handled using compensation techniques, however, vibrations and temperature gradients should be avoided whenever possible [168].

Clerici et al. [164] used laser triangulation to make 1D-measurements of the thickness change of a battery cell to validate an electrochemical-mechanical multi-scale model. The battery cells used in this study had an LFP cathode and a graphite anode, contained in a 70 mm by 27 mm by 180 mm prismatic case. The cell had a nominal capacity of 25 Ah. 1D-laser triangulation sensors were placed on either side of the 70 mm by 180 mm surface. The sensor used in this study has a measurement accuracy of 8 µm and an acquisition speed of 20 µs. At a discharge rate of 2C, the authors observed contractions up to 0.25 mm. During charge, a maximum increase in thickness of 0.25 mm was observed when performed at 1C. The authors observed similar maximum expansion and contraction values, even by varying charge rates from 0.1C to 1C, and discharge rates between 0.1C and 2C.

For 3D measurements, it is often necessary to scan the imaging spot over the part being imaged. This makes the acquisition time for 3D images significantly longer than for 1D images, as the part needs to be physically moved relative to the imaging spot. One approach to make 3D imaging faster is to make use of a line camera, as demonstrated by Rieger et al.. Rieger et al. demonstrated a 3D imaging approach where laser profile sensors are placed on either side of a pouch cell [165]. The profile sensors used are capable of simultaneously measuring distances over an 85 mm line projected onto the surface of the battery cell with an accuracy of 8 µm. A linear stage was then used to scan the pouch cell, yielding a 3D image of both sides of the pouch cell. Charging was performed using a CC-CV scheme at 1C at ambient temperatures of 17 °C, 25 °C, and 40 °C. In the tests at 17 °C and 25 °C, a local maximum in expansion was observed when the voltage of the cell reached 4.2 V, and charging transitioned to constant voltage mode. This local maximum was attributed to limited lithium diffusion at higher SoC. This effect was most significant in locations close to the tabs. After the transition to constant voltage charging, the cell contracts slightly, which the authors attribute to charge homogenization in the electrode. At all temperatures, the final average expansion at the end of charging was about 150 µm. The cells used in this study had a LCO cathode and a graphite anode with a capacity of 2.28 Ah, a cell thickness of 6.4 mm. Rieger's use of a line camera facilitated *in operando* 3D imaging, however the line implementation of laser triangulation systems are more complex, and therefore more costly, than their spot implementation counterparts.

Interferometric Measurements

In contrast to laser triangulation, which makes use of geometry to determine the location of an object, one could also exploit the interferometric nature of light to measure the position of a surface. Bohn et al. demonstrated a white light interferometry approach for measuring both small 2 Ah and larger 56 Ah cells [170,171]. White light interferometry is a coherent imaging technique, which requires a reference arm and a sample arm. In the simplest case, the light is split using a Michelson interferometer as demonstrated in Figure 13. When the optical path length difference between the reference arm and sample arm is less than the coherence length of the light source, an interference spectra will be observed at the detector. By observing shifts in the interference, one can determine the change in optical path length in the sample arm, and therefore the position of the object being measured. Even without additional fitting or averaging, the resolution can be in the range of single nanometers [172,173].

Bohn et al. [171] made use of a light emitting diode (LED) source with a coherence length of 12 µm, meaning that the measurement range is limited to the coherence length of the light source. A scanning component with a high resolution encoder was added to the sample arm to allow for measurements beyond the coherence length. Since the measurement was made by attaching a mirror to a free-moving metal block applying pressure to the cell, all measurements were taken on a single point. Expansion measurements of the battery cell were captured both from 0 % to 100 % SoC, but also over short 6 s pulses. The maximum cell expansion at full charge was approximately 200 µm, slowly increasing over 100 min. As such, the axial resolution was likely higher than required for this application. The high resolution of interferometric imaging was more useful for the measurements

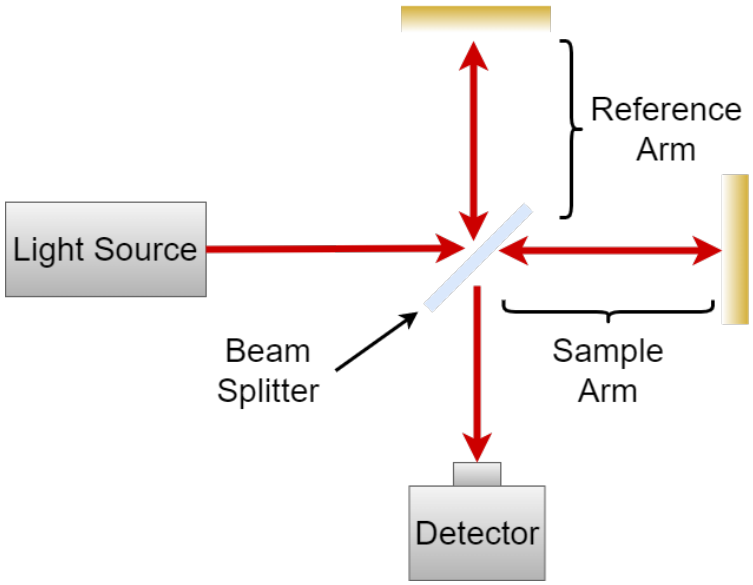

Figure 13. Michelson interferometer implementation of a white light measurement system. Figure reproduced without any changes from reference [174]

taken over 6 s, where expansions of only 0.2 µm were registered. This small expansion would not be quantifiable without a high resolution imaging system.

Yang et al. [175] made use of a different interferometric approach that has the capability of measuring multiple points on the surface instantaneously. Similar to white light interferometry, electronic speckle pattern interferometry electronic speckle pattern interferometry (ESPI) makes use of an interferometer with a reference arm and a sample arm. ESPI uses a diverging beam to illuminate the sample surface [176]. When the diverging beams from the reference and sample arm are recombined, the result is a fringe pattern on the detector camera. The intensity at each pixel as a function of time is given by

$$I(t) = I_0(t) + I_0(t)V\cos(\phi(t)) = I_0(t)\left(1 + V\cos\left(\phi_0 + \frac{4\pi z(t)}{\lambda}\right)\right) \tag{8}$$

where $I_0(t)$ is the speckle pattern intensity bias, V is the visibility of the surface being imaged, ϕ is the phase in the speckle pattern, ϕ_0 is the random phase, and $z(t)$ is the plane deformation of the surface being imaged [176]. Ultimately, $z(t)$ is the variable of interest, however V, ϕ_0, and $I_0(t)$ are often not precisely known at each pixel. To resolve this, a phase-shifting approach can be used to improve measurement sensitivity. The four-step phase shifting algorithm is implemented by taking four fringe patterns, each taken with a phase shift separated by $\pi/2$. The phase shift is typically implemented by using a piezoelectric stage to induce movements on the scale of a quarter of the wavelength of the light source for each subsequent image. This approach is only valid when the movement in the surface being interrogated is static in the time-scale of the frame rate of the camera. When implemented, this yields four intensities for each pixel: $I(t,0)$, $I(t,\pi/2)$, $I(t,\pi)$, $I(t,3\pi/2)$. We can combine the intensities to give

$$\phi(t) = \arctan\left(\frac{I(t,3\pi/2) - I(t,\pi/2)}{I(t,0) - I(t,\pi)}\right) \tag{9}$$

.

Filtering approaches can be applied to equation 9, followed by phase unwrapping, to extract the phase at a specific pixel. By determining the difference of $\phi(t_1)$ and $\phi(t_0)$, unwrapped phases at the same pixel taken at different times, one can then determine the displacement as long as one knows the wavelength of light being used for imaging.

Yang et al. [175] make use of an apparatus that is capable of measuring both sides of a pouch cell through the use of additional mirrors during imaging. Since battery expansion is relatively static on the scale of micrometers and the time scale of seconds, the authors were able to make use of the four-step-phase-shifting approach, leading to higher sensitivity. The authors were ultimately able to generate 3D images of both sides of cells with a sensitivity of under 10 µm.

Structured light

Another approach for achieving 3D-imaging of the expansion of battery cells is demonstrated by Rieger et al. through the use of structured light cameras [82]. Structured light cameras work by projecting a geometry on an object and then imaging this geometry. Any distortions in the geometry can be mapped as deviations from a flat plane. How these deviations are mapped to deformation depends on the selected geometry [177–179]. The selection of the geometry is application specific, and determines the complexity of calculating the distortion, accuracy, and the resolution of the resulting measurement. Geometries can be as simple as monochromatic stripes, or as complex as pseudo-random binary arrays [180]. The choice of geometry will determine whether measurements can be made using a multiple-shot, or a single-shot imaging scheme. Multiple-shot imaging is suitable for systems that are static in the time-scale of the frame rate, whereas single-shot approaches are necessary when considering measurements in dynamic systems [180–182].

Rieger et al. [82] made use of a structured light camera that projects multiple fringe projection geometries, and therefore requires multiple-shot imaging. Given the charge time of just over 90 min, and an acquisition time of 3 s, the cell expansion could be assumed to be effectively static during the acquisition. The measurements had a resolution in the direction perpendicular to the battery surface of 2 µm, and a distance of 60 µm between measurements in the plane of battery surface. By using 3D-imaging, the authors were able to identify that at lower SoC the expansion of the battery cell tended to have a more spatially homogeneous distribution, whereas at higher SoC the expansion showed variation across the surface. The obtained spatial resolution of the measurements was high, with 800,000 data points taken over the 60 mm x 50 mm surface.

Digital image correlation

Digital image correlation digital image correlation (DIC) is an imaging technique that has also been used to generate 3D-profiles of lithium-ion battery cells during cycling. Instead of projecting a geometry on the surface to be investigated, DIC makes use of existing, or applied texture on the surface to calculate displacement. The texture is typically created by coating the surface to be imaged in a speckled paint pattern. In DIC, measurements are typically all with reference to an initial reference measurement. By using at least two cameras, the displacement of the texture pattern in the vertical and horizontal directions can be computationally inferred. To extract the displacement of the surface, spatial cross-correlation calculations are required to match the real features on the surface in the images obtained from both cameras [183]. Temporal correlations can then be used to track features across frames taken by an individual camera. After cross-correlation, stereo-triangulation can be used to track the 3D-position of points in each feature as a function of time [184, 185]. Both cross-correlation and stereo-triangulation across the entire imaging field are computationally expensive procedures, though a number of researchers are attempting to improve performance [186–189]. As battery expansion is a relatively slow-moving process, DIC is still used by researchers to make measurements in this field.

Both Luo et al. [190] and Leung et al. [191], have demonstrated DIC for characterizing displacement and strain in lithium-ion batteries during cycling . Luo et al. took displacement and strain measurements over 55 cycles on a 54.5 mm by 56.5 mm LCO pouch cell. The measurements were taken at 1 Hz, though the measurement apparatus is capable of measurements up to 15 Hz. Leung et al. measured a maximum expansion of 197 µm at the end of charge during the 55th cycle. Similar work was demonstrated by Leung et al.,

however over fewer cycles and using a NMC pouch cell. The maximum displacement measured by Leung et al. was 200 µm.

4. Comparison of techniques

As outlined in section 3, there are a number of measurement approaches for characterizing the expansion of lithium-ion battery cells. There are a variety of factors that must be considered when selecting a measurement technique for a specific application. These factors could include the required information from the measurement, the effect of the measurement on the battery cell expansion, ease of use, footprint of the measurement device, required measurement range and resolution, and cost, among others.

As demonstrated in this review, the data collected to assess battery cell expansion is varied depending on what researchers are hoping to glean from the measurements. The goal of the measurement is an important consideration when selecting a suitable measurement technique. When simultaneous three dimensional measurements of the cell casing with high spatial resolution are desired, image based techniques, such as digital image correlation and structured light, or an electronic speckle pattern approach are likely the most suitable techniques. When simultaneous measurement is not required, techniques such as laser triangulation, or white light interferometry may be suitable. By implementing multiple sensors, dilatometry and strain-based measurements can also produce simultaneous three dimensional images, albeit with less spatial resolution. When the goal of the measurement is to observe expansion in individual components within the cell, one must use a radiological technique. If fast measurements are required, such that *in operando* measurements are possible, this will limit the selection to x-ray synchrotron or neutron beam sources.

Contact measurements, by their nature, require contact between sensor and battery cell which can influence the expansion behaviour. In the case of 1D-dilatometry measurements, displacement sensors are either in contact with the cell or electrode materials directly, or in contact with a surface, such as a pressure plate, that is in contact with the cell [20,47,52]. Though this type of sensor is typically designed to minimize the applied force by the probe, additional forces, however small, will be introduced into the system. Measurements made using both electrical and optical fiber strain gauges require the use of adhesive on the surface of the material being measured. Though effects are likely small, the adhesive layer on the surface could affect the measurement. Optical fiber strain sensors are often embedded in the cell, either on the surface of, or within the electrode. Placing the optical fiber in the cell causes the cell to perform differently than a cell without an embedded sensor [138,139]. This means that findings from these studies may not be transferable to standard cells without an embedded strain sensor. When considering buoyancy measurements, the expansion behaviour could be influenced due to the battery cell being submerged in oil. In contrast, non-contact measurements, such as those shown in the bottom tree in Figure 14, are at no risk of influencing the expansion measurement by introducing additional mechanical forces into the system. The greatest concern when considering the influences of non-contact measurements is introducing heat into the battery cell through the absorption and scattering of electromagnetic radiation or particles. In the case of radiological measurements that make use of x-rays, interactions between the beam and absorptive materials, such as the current collector, could cause heat input into the system [192]. In the case of neutron imaging, inelastic scattering, or absorption of the particle beam could have thermal influences. Optical imaging techniques can also heat the sample through the absorption of electromagnetic radiation. Thermal effects are minimized by limiting the energy that is transferred into the cell. For x-ray and neutron imaging, this is generally achieved by limiting exposure time. In optical measurements, low intensity light is used to minimize thermal effects.

The ease of use for a particular measurement technique can consider both the simplicity of installing the sensor for measurement, as well as how easily the relevant information can be extracted from the sensor data. Dilatometry and laser triangulation measurements are easy to implement, and the sensor data can be directly mapped to displacement with

minimal computational post processing. Techniques like strain, buoyancy, and digital image correlation measurement all have the disadvantage of contaminating the surface of the battery cell. In the case of strain measurements, the surface is contaminated with adhesive, with oil in the case of buoyancy measurements, and with paint in the case of digital image correlation. In addition, sensor outputs from these three techniques require additional information and calculation to extract battery expansion [108,119,120,125]. Both of the interferometric techniques outlined in this review are relatively complex to implement, and require significant post-processing to extract the relevant information [170,171,176]. Structured light imaging is relatively easy to implement, however the computation of deformation from the resulting images is complex and computationally expensive [184]. Radiological techniques are difficult to implement due to the shielding requirements to protect users from the resulting radiation. Generating the beams required for radiological approaches can also be challenging [192,193]. Finally, in the case of CT imaging, the computations required to construct a measurements are intensive.

Particularly when considering the simultaneous measurement of multiple cells, or measurement in confined spaces (such as in a temperature chamber), the footprint of the measurement device must be considered. Contact approaches such as dilatometry or strain gauge measurements can be achieved using a small measurement device placed directly on the part being measured. In contrast, methods such as laser triangulation and image based approaches require a specified offset from the battery cell, which must be accounted for when designing test environments for taking measurements. Radiological methods of measurement often have a large footprint due to the required shielding [192,193]. In addition, neutron sources and synchrotron sources for x-rays require entire separate facilities to supply the measurement beam [163,194].

Battery cells are diverse in their compositions, their size, and their internal structure. All of these characteristics will inform how much the cell is going to expand during both normal and abnormal operating conditions, as outlined in this review. In addition, some make measurements that are taken over an entire charge and discharge cycle, whereas others only investigate expansion over short timescales. When selecting the correct measuring approach, it is important to consider the maximum expansion one will need to measure, and to assess the required resolution of the measurement. Most of the measurement technologies presented in this review can be configured to have sufficient resolution and range for the measurement of expansion in battery cell casings. When one wants to measure very small deformations, such as those taken over short time scales, the options for measurement techniques are more limited.

Cost is a major consideration when selecting a measurement technique. Contact approaches tend to be less expensive than non-contact approaches. Measurement using x-ray synchrotron or neutron beam sources are prohibitively expensive for most applications, and use is typically confined to measurements made in an academic context. For the other techniques detailed in this review, the cost is highly dependent on the specification of the measurement system.

As demonstrated by the large body of academic literature presented in this review, dilatometry measurement approaches are the most prevalent. This is likely due to their ease of use, comparatively low cost, and configurable resolution and field of view.

5. Conclusions

This review strives to give a complete overview of the different techniques and technologies that are used to characterize volume expansion in lithium-ion battery cells. Prior to discussion of the measurement techniques, the different expansion mechanisms are explored. Reversible expansion due to lithium intercalation into and out of the electrodes during charging and discharging is considered in a variety of both established and up-and-coming electrode materials. Thermal expansion in lithium-ion battery cells is also discussed as a reversible expansion mechanism. It was also important to consider irreversible expansion mechanisms, as the causes of irreversible expansion can have negative effects on the

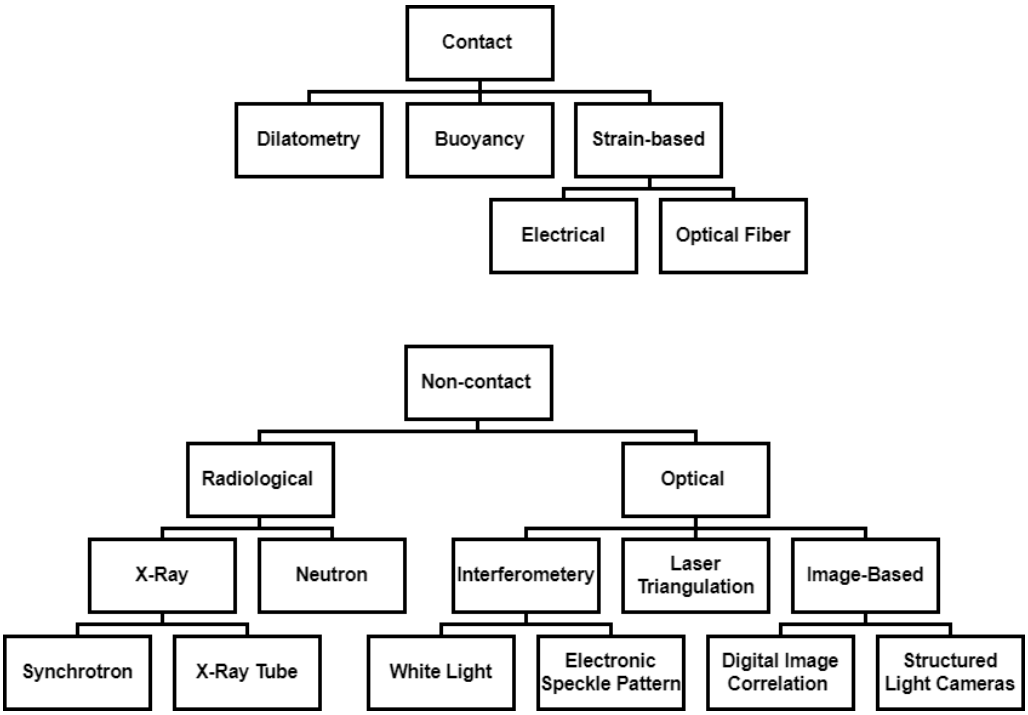

Figure 14. Tree diagrams outlining the numerous contact (top) and non-contact (bottom) approaches for measuring volume expansion in lithium-ion batteries, as covered in this publication

performance and safety of the cell. These expansion mechanisms include the formation of a SEI layer, lithium plating, and gas generation.

After establishing the causes of volume expansion in lithium-ion cells, methods for measuring expansion were considered. To better distinguish between different types of measurement, techniques were divided into contact and non-contact approaches. Contact approaches were further divided into dilatometry, strain gauge, and buoyancy based measurements. Dilatometry was, by a large margin, the most common method for characterizing volume expansion in the literature evaluated for this review. Non-contact approaches were further divided into radiological and optical measurements. Radiological measurements were generally only used when internal structures of either the cell or cell components were desired. Optical approaches were utilized to make both 1D and 3D contactless measurements of the surface of the cell.

Finally, the different measurement techniques were compared and contrasted according to a variety of factors that could be important when selecting an approach for characterizing the expansion of lithium-ion cells. The factors evaluated include the required information from the measurement, the effect of the measurement on the battery cell expansion, ease of use, footprint of the measurement device, required measurement range and resolution, and cost.

The lithium-ion battery cell is being used in increasingly demanding use cases ranging from green energy storage to electric mobility. As a result, there is increasing interest in both developing new cell chemistries, and the development of techniques for characterizing battery cells. The characterization of volume expansion in lithium-ion battery cells offers useful insights into the quality, safety, and performance capabilities. As such, it is likely that more measurement options will continue to be developed as we strive to better understand existing and next generation lithium-ion battery configurations.

Author Contributions: Conceptualization, X.X. and Y.Y.; investigation, T.K., D.N.; writing—original draft preparation, T.K., D.N.; writing—review and editing, T.K., D.N., L.P.B.; visualization, T.K., D.N.; supervision, C.H., M.V., M.S.; project administration, L.P.B.; funding acquisition, L.P.B., M.S.; All authors have read and agreed to the published version of the manuscript.

Funding: This research was funded by the Federal Ministry for economic affairs and climate action under the project acronym QUAZE and number 16BZF361B.

Conflicts of Interest: The authors declare no conflict of interest.

References

1. Geels, F.W. Disruption and low-carbon system transformation: Progress and new challenges in socio-technical transitions research and the Multi-Level Perspective. *Energy Research & Social Science* **2018**, *37*, 224–231. https://doi.org/10.1016/j.erss.2017.10.010.
2. Budde-Meiwes, H.; Drillkens, J.; Lunz, B.; Muennix, J.; Rothgang, S.; Kowal, J.; Sauer, D.U. A review of current automotive battery technology and future prospects. *Proceedings of the Institution of Mechanical Engineers, Part D: Journal of Automobile Engineering* **2013**, *227*, 761–776. https://doi.org/10.1177/0954407013485567.
3. Liu, Y.; Zhang, R.; Wang, J.; Wang, Y. Current and future lithium-ion battery manufacturing. *iScience* **2021**, *24*, 102332. https://doi.org/10.1016/j.isci.2021.102332.
4. Ren, D.; Xie, L.; Wang, L.; He, X. A practical approach to predict volume deformation of lithium–ion batteries from crystal structure changes of electrode materials. *Int J Energy Res* **2021**, *45*, 7732–7740. https://doi.org/10.1002/er.6355.
5. Siegel, J.B.; Stefanopoulou, A.G.; Hagans, P.; Ding, Y.; Gorsich, D. Expansion of Lithium Ion Pouch Cell Batteries: Observations from Neutron Imaging. *J. Electrochem. Soc.* **2013**, *160*, A1031–A1038. https://doi.org/10.1149/2.011308jes.
6. Heubner, C.; Schneider, M.; Michaelis, A. Detailed study of heat generation in porous LiCoO2 electrodes. *J. Power Sources* **2016**, *307*, 199–207. https://doi.org/10.1016/j.jpowsour.2015.12.096.
7. Liu, X.M.; Arnold, C.B. Effects of Cycling Ranges on Stress and Capacity Fade in Lithium-Ion Pouch Cells. *J. Electrochem. Soc.* **2016**, *163*, A2501–A2507. https://doi.org/10.1149/2.1131610jes.
8. Sturm, J.; Spingler, F.B.; Rieger, B.; Rheinfeld, A.; Jossen, A. Non-Destructive Detection of Local Aging in Lithium-Ion Pouch Cells by Multi-Directional Laser Scanning. *J. Electrochem. Soc.* **2017**, *164*, A1342–A1351. https://doi.org/10.1149/2.0161707jes.
9. Bernhard, R.; Metzger, M.; Gasteiger, H.A. Gas Evolution at Graphite Anodes Depending on Electrolyte Water Content and SEI Quality Studied by On-Line Electrochemical Mass Spectrometry. *J. Electrochem. Soc.* **2015**, *162*, A1984–A1989. https://doi.org/10.1149/2.0191510jes.
10. Deich, T.; Storch, M.; Steiner, K.; Bund, A. Effects of module stiffness and initial compression on lithium-ion cell aging Deich 2021 // Effects of module stiffness and initial compression on lithium-ion cell aging. *J. Power Sources* **2021**, *506*, 230163. https://doi.org/10.1016/j.jpowsour.2021.230163.
11. Deich, T.; Hahn, S.L.; Both, S.; Birke, K.P.; Bund, A. Validation of an actively-controlled pneumatic press to simulate automotive module stiffness for mechanically representative lithium-ion cell aging. *J Energy Storage* **2020**, *28*, 101192. https://doi.org/10.1016/j.est.2020.101192.
12. Mukhopadhyay, A.; Sheldon, B.W. Deformation and stress in electrode materials for Li-ion batteries. *Prog. Mater. Sci.* **2014**, *63*, 58–116. https://doi.org/10.1016/j.pmatsci.2014.02.001.
13. Nazari, P.; Bäuerle, R.; Zimmermann, J.; Melzer, C.; Schwab, C.; Smith, A.; Kowalsky, W.; Aghassi-Hagmann, J.; Hernandez-Sosa, G.; Lemmer, U. Piezoresistive Free-standing Microfiber Strain Sensor for High-resolution Battery Thickness Monitoring. *Adv. Mater.* **2023**, *35*, e2212189. https://doi.org/10.1002/adma.202212189.
14. Pfrang, A.; Kersys, A.; Kriston, A.; Scurtu, R.G.; Marinaro, M.; Wohlfahrt-Mehrens, M. Deformation from Formation Until End of Life: Micro X-ray Computed Tomography of Silicon Alloy Containing 18650 Li-Ion Cells. *J. Electrochem. Soc.* **2023**, *170*, 030548. https://doi.org/10.1149/1945-7111/acc6f3.
15. Piątek, J.; Afyon, S.; Budnyak, T.M.; Budnyk, S.; Sipponen, M.H.; Slabon, A. Sustainable Li–Ion Batteries: Chemistry and Recycling. *Adv. Energy Mater.* **2021**, *11*. https://doi.org/10.1002/aenm.202003456.
16. Adenusi, H.; Chass, G.A.; Passerini, S.; Tian, K.V.; Chen, G. Lithium Batteries and the Solid Electrolyte Interphase (SEI)—Progress and Outlook. *Adv. Energy Mater.* **2023**, *13*, 2203307. https://doi.org/10.1002/aenm.202203307.
17. Placke, T.; Kloepsch, R.; Dühnen, S.; Winter, M. Lithium ion, lithium metal, and alternative rechargeable battery technologies: the odyssey for high energy density. *J Solid State Electrochem* **2017**, *21*, 1939–1964. https://doi.org/10.1007/s10008-017-3610-7.
18. Das, D.; Manna, S.; Puravankara, S. Electrolytes, Additives and Binders for NMC Cathodes in Li-Ion Batteries—A Review. *Batteries* **2023**, *9*, 193. https://doi.org/10.3390/batteries9040193.
19. Graae, K.V.; Li, X.; Sørensen, D.R.; Ayerbe, E.; Boyano, I.; Sheptyakov, D.; Jørgensen, M.R.V.; Norby, P. Time and space resolved operando synchrotron X-ray and Neutron diffraction study of NMC811/Si–Gr 5 Ah pouch cells. *J. Power Sources* **2023**, *570*, 232993. https://doi.org/10.1016/j.jpowsour.2023.232993.
20. Bauer, M.; Wachtler, M.; Stöwe, H.; Persson, J.V.; Danzer, M.A. Understanding the dilation and dilation relaxation behavior of graphite-based lithium-ion cells. *J. Power Sources* **2016**, *317*, 93–102. https://doi.org/10.1016/j.jpowsour.2016.03.078.
21. Gantenbein, S.; Schönleber, M.; Weiss, M.; Ivers-Tiffée, E. Capacity Fade in Lithium-Ion Batteries and Cyclic Aging over Various State-of-Charge Ranges. *Sustainability* **2019**, *11*, 6697. https://doi.org/10.3390/su11236697.
22. Sethuraman, V.A.; Hardwick, L.J.; Srinivasan, V.; Kostecki, R. Surface structural disordering in graphite upon lithium intercalation/deintercalation. *J. Power Sources* **2010**, *195*, 3655–3660. https://doi.org/10.1016/j.jpowsour.2009.12.034.

23. Nitta, N.; Wu, F.; Lee, J.T.; Yushin, G. Li-ion battery materials: present and future. *Mater. Today* **2015**, *18*, 252–264. https://doi.org/10.1016/j.mattod.2014.10.040.
24. Birkenmaier, C.; Bitzer, B.; Harzheim, M.; Hintennach, A.; Schleid, T. Lithium Plating on Graphite Negative Electrodes: Innovative Qualitative and Quantitative Investigation Methods. *J. Electrochem. Soc.* **2015**, *162*, A2646–A2650. https://doi.org/10.1149/2.0451514jes.
25. Mercer, M.P.; Peng, C.; Soares, C.; Hoster, H.E.; Kramer, D. Voltage hysteresis during lithiation/delithiation of graphite associated with meta-stable carbon stackings. *J. Mater. Chem. A* **2021**, *9*, 492–504. https://doi.org/10.1039/D0TA10403E.
26. Clerici, D.; Mocera, F.; Somà, A. Experimental Characterization of Lithium-Ion Cell Strain Using Laser Sensors. *Energies* **2021**, *14*, 6281. https://doi.org/10.3390/en14196281.
27. Asenbauer, J.; Eisenmann, T.; Kuenzel, M.; Kazzazi, A.; Chen, Z.; Bresser, D. The success story of graphite as a lithium-ion anode material – fundamentals, remaining challenges, and recent developments including silicon (oxide) composites. *Sustainable Energy & Fuels* **2020**, *4*, 5387–5416. https://doi.org/10.1039/D0SE00175A.
28. Ghosh, A.; Ghamouss, F. Role of Electrolytes in the Stability and Safety of Lithium Titanate-Based Batteries. *Front. Mater.* **2020**, *7*. https://doi.org/10.3389/fmats.2020.00186.
29. Lv, W.; Gu, J.; Niu, Y.; Wen, K.; He, W. Review—Gassing Mechanism and Suppressing Solutions in Li 4 Ti 5 O 12 -Based Lithium-Ion Batteries. *J. Electrochem. Soc.* **2017**, *164*, A2213–A2224. https://doi.org/10.1149/2.0031712jes.
30. Han, C.; He, Y.B.; Liu, M.; Li, B.; Yang, Q.H.; Wong, C.P.; Kang, F. A review of gassing behavior in Li 4 Ti 5 O 12 -based lithium ion batteries. *J. Mater. Chem. A* **2017**, *5*, 6368–6381. https://doi.org/10.1039/C7TA00303J.
31. He, Y.B.; Li, B.; Liu, M.; Zhang, C.; Lv, W.; Yang, C.; Li, J.; Du, H.; Zhang, B.; Yang, Q.H.; et al. Gassing in Li(4)Ti(5)O(12)-based batteries and its remedy. *Sci Rep* **2012**, *2*, 913. https://doi.org/10.1038/srep00913.
32. Sauerteig, D.; Ivanov, S.; Reinshagen, H.; Bund, A. Reversible and irreversible dilation of lithium-ion battery electrodes investigated by in-situ dilatometry. *J. Power Sources* **2017**, *342*, 939–946. https://doi.org/10.1016/j.jpowsour.2016.12.121.
33. Nemeth, T.; Schröer, P.; Kuipers, M.; Sauer, D.U. Lithium titanate oxide battery cells for high-power automotive applications – Electro-thermal properties, aging behavior and cost considerations. *J Energy Storage* **2020**, *31*, 101656. https://doi.org/10.1016/j.est.2020.101656.
34. Song, T.; Jeon, Y.; Paik, U. Si nanotubes array sheathed with SiN/SiOxNy layer as an anode material for lithium ion batteries. *Journal of Electroceramics* **2014**, *32*, 66–71. https://doi.org/10.1007/s10832-013-9871-3.
35. Zhang, X.; Weng, J.; Ye, C.; Liu, M.; Wang, C.; Wu, S.; Tong, Q.; Zhu, M.; Gao, F. Strategies for Controlling or Releasing the Influence Due to the Volume Expansion of Silicon inside Si-C Composite Anode for High-Performance Lithium-Ion Batteries. *Materials* **2022**, *15*. https://doi.org/10.3390/ma15124264.
36. Shen, T.; Yao, Z.; Xia, X.; Wang, X.; Gu, C.; Tu, J. Rationally Designed Silicon Nanostructures as Anode Material for Lithium–Ion Batteries. *Adv Eng Mater* **2018**, *20*. https://doi.org/10.1002/adem.201700591.
37. Liu, X.; Zhu, X.; Pan, D. Solutions for the problems of silicon-carbon anode materials for lithium-ion batteries. *R. Soc. open sci.* **2018**, *5*, 172370. https://doi.org/10.1098/rsos.172370.
38. Zuo, X.; Zhu, J.; Müller-Buschbaum, P.; Cheng, Y.J. Silicon based lithium-ion battery anodes: A chronicle perspective review. *Nano Energy* **2017**, *31*, 113–143. https://doi.org/10.1016/j.nanoen.2016.11.013.
39. Zhao, X.; Lehto, V.P. Challenges and prospects of nanosized silicon anodes in lithium-ion batteries. *Nanotechnology* **2021**, *32*, 042002. https://doi.org/10.1088/1361-6528/abb850.
40. Dou, F.; Weng, Y.; Wang, Q.; Chen, G.; Liu, H.; Shi, L.; Zhang, D. In situ imaging analysis of the inhibition effect of functional coating on the volume expansion of silicon anodes. *Chemical Engineering Journal* **2021**, *417*, 128122. https://doi.org/10.1016/j.cej.2020.128122.
41. Luo, W.; Chen, X.; Xia, Y.; Chen, M.; Wang, L.; Wang, Q.; Li, W.; Yang, J. Surface and Interface Engineering of Silicon–Based Anode Materials for Lithium–Ion Batteries. *Advanced Energy Materials* **2017**, *7*. https://doi.org/10.1002/aenm.201701083.
42. Popp, H.; Koller, M.; Jahn, M.; Bergmann, A. Mechanical methods for state determination of Lithium-Ion secondary batteries: A review. *J Energy Storage* **2020**, *32*, 101859. https://doi.org/10.1016/j.est.2020.101859.
43. Noerochim, L.; Suwarno, S.; Idris, N.H.; Dipojono, H.K. Recent Development of Nickel-Rich and Cobalt-Free Cathode Materials for Lithium-Ion Batteries. *Batteries* **2021**, *7*, 84. https://doi.org/10.3390/batteries7040084.
44. Rieger, B.; Schlueter, S.; Erhard, S.V.; Jossen, A. Strain Propagation in Lithium-Ion Batteries from the Crystal Structure to the Electrode Level. *J. Electrochem. Soc.* **2016**, *163*, A1595–A1606. https://doi.org/10.1149/2.0431608jes.
45. Li, L.; Luo, C.; Zou, J.; Ran, Q.; Chen, P.; Wang, X.; Zhao, Y.; Wang, L.; Zheng, J.; Niu, X. Prelithiated FeS2 cathode with alleviated volume expansion toward improved cycling performance. *Solid State Ionics* **2021**, *368*, 115696. https://doi.org/10.1016/j.ssi.2021.115696.
46. Mao, C.; An, S.J.; Meyer, H.M.; Li, J.; Wood, M.; Ruther, R.E.; Wood, D.L. Balancing formation time and electrochemical performance of high energy lithium-ion batteries. *J. Power Sources* **2018**, *402*, 107–115. https://doi.org/10.1016/j.jpowsour.2018.09.019.
47. Hemmerling, J.; Guhathakurta, J.; Dettinger, F.; Fill, A.; Birke, K.P. Non-Uniform Circumferential Expansion of Cylindrical Li-Ion Cells—The Potato Effect. *Batteries* **2021**, *7*, 61. https://doi.org/10.3390/batteries7030061.
48. Zhang, X.; He, J.; Zhou, J.; Chen, H.; Song, W.; Fang, D. Thickness evolution of commercial Li-ion pouch cells with silicon-based composite anodes and NCA cathodes. *Sci. China Technol. Sci.* **2021**, *64*, 83–90. https://doi.org/10.1007/s11431-020-1709-y.

49. Li, T.; Yuan, X.Z.; Zhang, L.; Song, D.; Shi, K.; Bock, C. Degradation Mechanisms and Mitigation Strategies of Nickel-Rich NMC-Based Lithium-Ion Batteries. *Electrochem. Energ. Rev.* **2020**, *3*, 43–80. https://doi.org/10.1007/s41918-019-00053-3.
50. Zhang, G.; Li, M.; Ye, Z.; Chen, T.; Cao, J.; Yang, H.; Ma, C.; Jia, Z.; Xie, J.; Cui, N.; et al. Lithium Iron Phosphate and Layered Transition Metal Oxide Cathode for Power Batteries: Attenuation Mechanisms and Modification Strategies. *Materials* **2023**, *16*. https://doi.org/10.3390/ma16175769.
51. Mei, W.; Duan, Q.; Lu, W.; Sun, J.; Wang, Q. An investigation on expansion behavior of lithium ion battery based on the thermal-mechanical coupling model. *J Clean Prod* **2020**, *274*, 122643. https://doi.org/10.1016/j.jclepro.2020.122643.
52. Vorwerk, P.; Hahn, S.K.; Daniel, C.; Krause, U.; Keutel, K. Detection of Critical Conditions in Pouch Cells Based on Their Expansion Behavior. *Batteries* **2022**, *8*, 42. https://doi.org/10.3390/batteries8050042.
53. Oh, K.Y.; Epureanu, B.I. A novel thermal swelling model for a rechargeable lithium-ion battery cell. *J. Power Sources* **2016**, *303*, 86–96. https://doi.org/10.1016/j.jpowsour.2015.10.085.
54. Liu, G.; Ouyang, M.; Lu, L.; Li, J.; Han, X. Analysis of the heat generation of lithium-ion battery during charging and discharging considering different influencing factors. *J Therm Anal Calorim* **2014**, *116*, 1001–1010. https://doi.org/10.1007/s10973-013-3599-9.
55. Piłatowicz, G.; Marongiu, A.; Drillkens, J.; Sinhuber, P.; Sauer, D.U. A critical overview of definitions and determination techniques of the internal resistance using lithium-ion, lead-acid, nickel metal-hydride batteries and electrochemical double-layer capacitors as examples. *J. Power Sources* **2015**, *296*, 365–376. https://doi.org/10.1016/j.jpowsour.2015.07.073.
56. Yoo, K.; Kim, J. Thermal behavior of full-scale battery pack based on comprehensive heat-generation model. *J. Power Sources* **2019**, *433*, 226715. https://doi.org/10.1016/j.jpowsour.2019.226715.
57. Zhai, Q.; Xu, X.; Kong, J.; Liu, M.; Xu, P.; Heidarshenas, B.; Wang, Q.; Zhou, F.; Wei, H. 3D Simulation Study on Thermal Behavior and Thermal Stress of Lithium–Ion Battery. *Energy Tech* **2023**, *11*. https://doi.org/10.1002/ente.202200795.
58. Mei, W.; Chen, H.; Sun, J.; Wang, Q. Numerical study on tab dimension optimization of lithium-ion battery from the thermal safety perspective. *Appl. Therm. Eng.* **2018**, *142*, 148–165. https://doi.org/10.1016/j.applthermaleng.2018.06.075.
59. Wang, S. Entropy and heat generation of lithium cells/batteries. *Chinese Physics B* **2016**, *25*, 010509. https://doi.org/10.1088/1674-1056/25/1/010509.
60. Bree, G.; Hao, H.; Stoeva, Z.; John Low, C.T. Monitoring state of charge and volume expansion in lithium-ion batteries: an approach using surface mounted thin-film graphene sensors. *RSC advances* **2023**, *13*, 7045–7054. https://doi.org/10.1039/d2ra07572e.
61. McBrayer, J.D.; Apblett, C.A.; Harrison, K.L.; Fenton, K.R.; Minteer, S.D. Mechanical studies of the solid electrolyte interphase on anodes in lithium and lithium ion batteries. *Nanotechnology* **2021**, *32*, 502005. https://doi.org/10.1088/1361-6528/ac17fe.
62. Jankowski, P.; Wieczorek, W.; Johansson, P. SEI-forming electrolyte additives for lithium-ion batteries: development and benchmarking of computational approaches. *J Mol Model* **2017**, *23*, 6. https://doi.org/10.1007/s00894-016-3180-0.
63. Zhao, X.; Chen, Y.; Sun, H.; Yuan, T.; Gong, Y.; Liu, X.; Chen, T. Impact of Surface Structure on SEI for Carbon Materials in Alkali Ion Batteries: A Review. *Batteries* **2023**, *9*, 226. https://doi.org/10.3390/batteries9040226.
64. Zhu, T.; Hu, Q.; Yan, G.; Wang, J.; Wang, Z.; Guo, H.; Li, X.; Peng, W. Manipulating the Composition and Structure of Solid Electrolyte Interphase at Graphite Anode by Adjusting the Formation Condition. *Energy Tech* **2019**, *7*, 1900273. https://doi.org/10.1002/ente.201900273.
65. Schomburg, F.; Drees, R.; Kurrat, M.; Danzer, M.A.; Röder, F. Characterization of the Solid–Electrolyte Interphase Growth During Cell Formation Based on Differential Voltage Analysis. *Energy Tech* **2023**, *11*. https://doi.org/10.1002/ente.202200688.
66. Peled, E.; Menkin, S. Review—SEI: Past, Present and Future. *J. Electrochem. Soc.* **2017**, *164*, A1703–A1719. https://doi.org/10.1149/2.1441707jes.
67. Louli, A.J.; Ellis, L.D.; Dahn, J.R. Operando Pressure Measurements Reveal Solid Electrolyte Interphase Growth to Rank Li-Ion Cell Performance. *Joule* **2019**, *3*, 745–761. https://doi.org/10.1016/j.joule.2018.12.009.
68. Pinson, M.B.; Bazant, M.Z. Theory of SEI Formation in Rechargeable Batteries: Capacity Fade, Accelerated Aging and Lifetime Prediction. *J. Electrochem. Soc.* **2013**, *160*, A243–A250. https://doi.org/10.1149/2.044302jes.
69. Bitzer, B.; Gruhle, A. A new method for detecting lithium plating by measuring the cell thickness. *J. Power Sources* **2014**, *262*, 297–302. https://doi.org/10.1016/j.jpowsour.2014.03.142.
70. Cannarella, J.; Arnold, C.B. The Effects of Defects on Localized Plating in Lithium-Ion Batteries. *J. Electrochem. Soc.* **2015**, *162*, A1365–A1373. https://doi.org/10.1149/2.1051507jes.
71. Janakiraman, U.; Garrick, T.R.; Fortier, M.E. Review—Lithium Plating Detection Methods in Li-Ion Batteries. *J. Electrochem. Soc.* **2020**, *167*, 160552. https://doi.org/10.1149/1945-7111/abd3b8.
72. Lin, X.; Khosravinia, K.; Hu, X.; Li, J.; Lu, W. Lithium Plating Mechanism, Detection, and Mitigation in Lithium-Ion Batteries. *Prog Energy Combust Sci.* **2021**, *87*, 100953. https://doi.org/10.1016/j.pecs.2021.100953.
73. Waldmann, T.; Hogg, B.I.; Wohlfahrt-Mehrens, M. Li plating as unwanted side reaction in commercial Li-ion cells – A review. *J. Power Sources* **2018**, *384*, 107–124. https://doi.org/10.1016/j.jpowsour.2018.02.063.
74. Münster, P.; Diehl, M.; Frerichs, J.E.; Börner, M.; Hansen, M.R.; Winter, M.; Niehoff, P. Effect of Li plating during formation of lithium ion batteries on their cycling performance and thermal safety. *J. Power Sources* **2021**, *484*, 229306. https://doi.org/10.1016/j.jpowsour.2020.229306.
75. Rowden, B.; Garcia-Araez, N. A review of gas evolution in lithium ion batteries. *Energy Reports* **2020**, *6*, 10–18. https://doi.org/10.1016/j.egyr.2020.02.022.

76. James, J.D.; Spittle, J.A.; Brown, S.G.R.; Evans, R.W. A review of measurement techniques for the thermal expansion coefficient of metals and alloys at elevated temperatures. *Meas. Sci. Technol.* **2001**, *12*, R1–R15. https://doi.org/10.1088/0957-0233/12/3/201.
77. Michael, H.; Jervis, R.; Brett, D.J.L.; Shearing, P.R. Developments in Dilatometry for Characterisation of Electrochemical Devices. *Batteries & Supercaps* **2021**, *4*, 1378–1396. https://doi.org/10.1002/batt.202100027.
78. Moyassari, E.; Roth, T.; Kücher, S.; Chang, C.C.; Hou, S.C.; Spingler, F.B.; Jossen, A. The Role of Silicon in Silicon-Graphite Composite Electrodes Regarding Specific Capacity, Cycle Stability, and Expansion. *J. Electrochem. Soc.* **2022**, *169*, 010504. https://doi.org/10.1149/1945-7111/ac4545.
79. Biberacher, W.; Lerf, A.; Besenhard, J.O.; Möhwald, H.; Butz, T. A high resolution dilatometer for in situ studies of the electrointercalation of layered materials. *Materials Research Bulletin* **1982**, *17*, 1385–1392. https://doi.org/10.1016/0025-5408(82)90223-9.
80. Huesker, J.; Froböse, L.; Kwade, A.; Winter, M.; Placke, T. In Situ Dilatometric Study of the Binder Influence on the Electrochemical Intercalation of Bis(trifluoromethanesulfonyl) imide Anions into Graphite. *Electrochimica Acta* **2017**, *257*, 423–435. https://doi.org/10.1016/j.electacta.2017.10.042.
81. Bazlen, S.; Heugel, P.; von Kessel, O.; Commerell, W.; Tübke, J. Influence of charging protocols on the charging capability and aging of lithium-ion cells with silicon-containing anodes. *Journal of Energy Storage* **2022**, *49*, 104044. https://doi.org/10.1016/j.est.2022.104044.
82. Rieger, B.; Schlueter, S.; Erhard, S.V.; Schmalz, J.; Reinhart, G.; Jossen, A. Multi-scale investigation of thickness changes in a commercial pouch type lithium-ion battery. *J. Energy Storage* **2016**, *6*, 213–221. https://doi.org/10.1016/j.est.2016.01.006.
83. Göttlinger, M.; Daubinger, P.; Stracke, W.; Hartmann, S.; Giffin, G.A. Influence of external pressure on silicon electrodes in lithium-ion cells. *Electrochimica Acta* **2022**, *419*, 140354. https://doi.org/10.1016/j.electacta.2022.140354.
84. Cannarella, J.; Arnold, C.B. Stress evolution and capacity fade in constrained lithium-ion pouch cells. *J. Power Sources* **2014**, *245*, 745–751. https://doi.org/10.1016/j.jpowsour.2013.06.165.
85. Oh, K.Y.; Epureanu, B.I.; Siegel, J.B.; Stefanopoulou, A.G. Phenomenological force and swelling models for rechargeable lithium-ion battery cells. *J. Power Sources* **2016**, *310*, 118–129. https://doi.org/10.1016/j.jpowsour.2016.01.103.
86. Chae, S.; Ko, M.; Kim, K.; Ahn, K.; Cho, J. Confronting Issues of the Practical Implementation of Si Anode in High-Energy Lithium-Ion Batteries. *Joule* **2017**, *1*, 47–60. https://doi.org/10.1016/j.joule.2017.07.006.
87. Grimsmann, F.; Brauchle, F.; Gerbert, T.; Gruhle, A.; Knipper, M.; Parisi, J. Hysteresis and current dependence of the thickness change of lithium-ion cells with graphite anode. *J Energy Storage* **2017**, *12*, 132–137. https://doi.org/10.1016/j.est.2017.04.006.
88. Jahn, L.; Katzer, F.; Danzer, M.A. Combined dilatometry and voltage analysis for a reliable detection of lithium deposition on graphitic anodes. *J. Power Sources* **2022**, *520*, 230870. https://doi.org/10.1016/j.jpowsour.2021.230870.
89. Michelini, E.; Höschele, P.; Heindl, S.F.; Erker, S.; Ellersdorfer, C. Experimental Investigation on Reversible Swelling Mechanisms of Lithium-Ion Batteries under a Varying Preload Force. *Batteries* **2023**, *9*, 218. https://doi.org/10.3390/batteries9040218.
90. Mohtat, P.; Lee, S.; Siegel, J.B.; Stefanopoulou, A.G. Towards better estimability of electrode-specific state of health: Decoding the cell expansion. *J. Power Sources* **2019**, *427*, 101–111. https://doi.org/10.1016/j.jpowsour.2019.03.104.
91. Müller, V.; Scurtu, R.G.; Richter, K.; Waldmann, T.; Memm, M.; Danzer, M.A.; Wohlfahrt-Mehrens, M. Effects of Mechanical Compression on the Aging and the Expansion Behavior of Si/C-Composite | NMC811 in Different Lithium-Ion Battery Cell Formats. *J. Electrochem. Soc.* **2019**, *166*, A3796–A3805. https://doi.org/10.1149/2.1121915jes.
92. Nagayama, M.; Ariyoshi, K.; Yamamoto, Y.; Ohzuku, T. Characterization of Lithium Insertion Electrodes by Precision Dilatometer: Area-Specific Deformation of Single Electrode. *J. Electrochem. Soc.* **2014**, *161*, A1388–A1393. https://doi.org/10.1149/2.0981409jes.
93. Sauerteig, D.; Hanselmann, N.; Arzberger, A.; Reinshagen, H.; Ivanov, S.; Bund, A. Electrochemical-mechanical coupled modeling and parameterization of swelling and ionic transport in lithium-ion batteries. *J. Power Sources* **2018**, *378*, 235–247. https://doi.org/10.1016/j.jpowsour.2017.12.044.
94. Schmider, D.; Bessler, W.G. Thermo-Electro-Mechanical Modeling and Experimental Validation of Thickness Change of a Lithium-Ion Pouch Cell with Blend Positive Electrode. *Batteries* **2023**, *9*, 354. https://doi.org/10.3390/batteries9070354.
95. Stock, S.; Diller, F.; Böhm, J.; Hille, L.; Hagemeister, J.; Sommer, A.; Daub, R. Operando Analysis of the Gassing and Swelling Behavior of Lithium-ion Pouch Cells during Formation. *J. Electrochem. Soc.* **2023**, *170*, 060539. https://doi.org/10.1149/1945-7111/acde0f.
96. Grimsmann, F.; Gerbert, T.; Brauchle, F.; Gruhle, A.; Parisi, J.; Knipper, M. Determining the maximum charging currents of lithium-ion cells for small charge quantities. *J. Power Sources* **2017**, *365*, 12–16. https://doi.org/10.1016/j.jpowsour.2017.08.044.
97. Waluś, S.; Offer, G.; Hunt, I.; Patel, Y.; Stockley, T.; Williams, J.; Purkayastha, R. Volumetric expansion of Lithium-Sulfur cell during operation – Fundamental insight into applicable characteristics. *Energy Stor. Mater.* **2018**, *10*, 233–245. https://doi.org/10.1016/j.ensm.2017.05.017.
98. Lee, J.H.; Lee, H.M.; Ahn, S. Battery dimensional changes occurring during charge/discharge cycles—thin rectangular lithium ion and polymer cells. *J. Power Sources* **2003**, *119-121*, 833–837. https://doi.org/10.1016/S0378-7753(03)00281-7.
99. Louli, A.J.; Li, J.; Trussler, S.; Fell, C.R.; Dahn, J.R. Volume, Pressure and Thickness Evolution of Li-Ion Pouch Cells with Silicon-Composite Negative Electrodes. *J. Electrochem. Soc.* **2017**, *164*, A2689–A2696. https://doi.org/10.1149/2.1691712jes.
100. Berckmans, G.; de Sutter, L.; Marinaro, M.; Smekens, J.; Jaguemont, J.; Wohlfahrt-Mehrens, M.; van Mierlo, J.; Omar, N. Analysis of the effect of applying external mechanical pressure on next generation silicon alloy lithium-ion cells. *Electrochimica Acta* **2019**, *306*, 387–395. https://doi.org/10.1016/j.electacta.2019.03.138.

101. Yoon, D.h.; Marinaro, M.; Axmann, P.; Wohlfahrt-Mehrens, M. Communication—Quantitative Analysis of Consumption of Fluoroethylene Carbonate Additives on Silicon Alloy Anodes. *J. Electrochem. Soc.* **2018**, *165*, A2467–A2469. https://doi.org/10.1149/2.0301811jes.
102. Marinaro, M.; Yoon, D.h.; Gabrielli, G.; Stegmaier, P.; Figgemeier, E.; Spurk, P.C.; Nelis, D.; Schmidt, G.; Chauveau, J.; Axmann, P.; et al. High performance 1.2 Ah Si-alloy/Graphite | LiNi 0.5 Mn 0.3 Co 0.2 O 2 prototype Li-ion battery. *J. Power Sources* **2017**, *357*, 188–197. https://doi.org/10.1016/j.jpowsour.2017.05.010.
103. Wang, Y.; Zhang, Q.; Li, D.; Hu, J.; Xu, J.; Dang, D.; Xiao, X.; Cheng, Y.T. Mechanical Property Evolution of Silicon Composite Electrodes Studied by Environmental Nanoindentation. *Advanced Energy Materials* **2018**, *8*. https://doi.org/10.1002/aenm.201702578.
104. Li, J.Y.; Xu, Q.; Li, G.; Yin, Y.X.; Wan, L.J.; Guo, Y.G. Research progress regarding Si-based anode materials towards practical application in high energy density Li-ion batteries. *Materials Chemistry Frontiers* **2017**, *1*, 1691–1708. https://doi.org/10.1039/C6QM00302H.
105. Jin, C.; Wang, Y.; Borujerdi, A.S.; Li, J. Stress evolution and thickness change of a lithium-ion pouch cell under various cycling conditions. *Journal of Power Sources Advances* **2022**, *16*, 100103. https://doi.org/10.1016/j.powera.2022.100103.
106. Grimsmann, F.; Brauchle, F.; Gerbert, T.; Gruhle, A.; Parisi, J.; Knipper, M. Impact of different aging mechanisms on the thickness change and the quick-charge capability of lithium-ion cells. *J Energy Storage* **2017**, *14*, 158–162. https://doi.org/10.1016/j.est.2017.10.010.
107. Oh, K.Y.; Siegel, J.B.; Secondo, L.; Kim, S.U.; Samad, N.A.; Qin, J.; Anderson, D.; Garikipati, K.; Knobloch, A.; Epureanu, B.I.; et al. Rate dependence of swelling in lithium-ion cells. *J. Power Sources* **2014**, *267*, 197–202. https://doi.org/10.1016/j.jpowsour.2014.05.039.
108. Aiken, C.P.; Xia, J.; Wang, D.Y.; Stevens, D.A.; Trussler, S.; Dahn, J.R. An Apparatus for the Study of In Situ Gas Evolution in Li-Ion Pouch Cells. *J. Electrochem. Soc.* **2014**, *161*, A1548–A1554. https://doi.org/10.1149/2.0151410jes.
109. Leißing, M.; Horsthemke, F.; Wiemers-Meyer, S.; Winter, M.; Niehoff, P.; Nowak, S. The Impact of the C–Rate on Gassing During Formation of NMC622 II Graphite Lithium–Ion Battery Cells. *Batteries & Supercaps* **2021**, *4*, 1344–1350. https://doi.org/10.1002/batt.202100056.
110. Self, J.; Aiken, C.P.; Petibon, R.; Dahn, J.R. Survey of Gas Expansion in Li-Ion NMC Pouch Cells. *J. Electrochem. Soc.* **2015**, *162*, A796–A802. https://doi.org/10.1149/2.0081506jes.
111. Liu, Q.Q.; Xiong, D.J.; Petibon, R.; Du, C.Y.; Dahn, J.R. Gas Evolution during Unwanted Lithium Plating in Li-Ion Cells with EC-Based or EC-Free Electrolytes. *J. Electrochem. Soc.* **2016**, *163*, A3010–A3015. https://doi.org/10.1149/2.0711614jes.
112. Xiong, D.J.; Petibon, R.; Madec, L.; Hall, D.S.; Dahn, J.R. Some Effects of Intentionally Added Water on LiCoO 2 /Graphite Pouch Cells. *J. Electrochem. Soc.* **2016**, *163*, A1678–A1685. https://doi.org/10.1149/2.0901608jes.
113. Ellis, L.D.; Allen, J.P.; Thompson, L.M.; Harlow, J.E.; Stone, W.J.; Hill, I.G.; Dahn, J.R. Quantifying, Understanding and Evaluating the Effects of Gas Consumption in Lithium-Ion Cells. *J. Electrochem. Soc.* **2017**, *164*, A3518–A3528. https://doi.org/10.1149/2.0191714jes.
114. Krause, L.J.; Chevrier, V.L.; Jensen, L.D.; Brandt, T. The Effect of Carbon Dioxide on the Cycle Life and Electrolyte Stability of Li-Ion Full Cells Containing Silicon Alloy. *J. Electrochem. Soc.* **2017**, *164*, A2527–A2533. https://doi.org/10.1149/2.1121712jes.
115. Milien, M.S.; Hoffmann, J.; Payne, M.; Lucht, B.L. Effect of Electrolyte Additives on Li 4 Ti 5 O 12 Cycling Performance and Gas Evolution. *J. Electrochem. Soc.* **2018**, *165*, A3925–A3931. https://doi.org/10.1149/2.0741816jes.
116. Guillot, S.L.; Usrey, M.L.; Peña-Hueso, A.; Kerber, B.M.; Zhou, L.; Du, P.; Johnson, T. Reduced Gassing In Lithium-Ion Batteries With Organosilicon Additives. *J. Electrochem. Soc.* **2021**, *168*, 030533. https://doi.org/10.1149/1945-7111/abed25.
117. Rodrigues, M.T.F.; Trask, S.E.; Shkrob, I.A.; Abraham, D.P. Quantifying gas generation from slurries used in fabrication of Si-containing electrodes for lithium-ion cells. *J. Power Sources* **2018**, *395*, 289–294. https://doi.org/10.1016/j.jpowsour.2018.05.071.
118. Peng, J.; Zhou, X.; Jia, S.; Jin, Y.; Xu, S.; Chen, J. High precision strain monitoring for lithium ion batteries based on fiber Bragg grating sensors. *J. Power Sources* **2019**, *433*, 226692. https://doi.org/10.1016/j.jpowsour.2019.226692.
119. Hickey, R.; Jahns, T.M. Measuring Individual Battery Dimensional Changes for State-of-Charge Estimation using Strain Gauge Sensors. In Proceedings of the ECCE 2019, Piscataway, NJ, 2019; pp. 2460–2465. https://doi.org/10.1109/ECCE.2019.8912578.
120. Choi, W.; Seo, Y.; Yoo, K.; Ko, T.J.; Choi, J. Carbon Nanotube-Based Strain Sensor for Excessive Swelling Detection of Lithium-Ion Battery. In Proceedings of the 2019 20th International Conference on Solid-State Sensors, Actuators and Microsystems & Eurosensors XXXIII (TRANSDUCERS & EUROSENSORS XXXIII). IEEE, 2019, pp. 2356–2359. https://doi.org/10.1109/TRANSDUCERS.2019.8808477.
121. Willenberg, L.K.; Dechent, P.; Fuchs, G.; Sauer, D.U.; Figgemeier, E. High-Precision Monitoring of Volume Change of Commercial Lithium-Ion Batteries by Using Strain Gauges. *Sustainability* **2020**, *12*, 557. https://doi.org/10.3390/su12020557.
122. Wahl, M.S.; Spitthoff, L.; Muri, H.I.; Jinasena, A.; Burheim, O.S.; Lamb, J.J. The Importance of Optical Fibres for Internal Temperature Sensing in Lithium-ion Batteries during Operation. *Energies* **2021**, *14*, 3617. https://doi.org/10.3390/en14123617.
123. Du, W.; Tao, X.M.; Tam, H.Y.; Choy, C.L. Fundamentals and applications of optical fiber Bragg grating sensors to textile structural composites. *Composite Structures* **1998**, *42*, 217–229. https://doi.org/10.1016/S0263-8223(98)00045-2.
124. Helsztynski, J.; Lewandowski, L.; Jasiewicz, W.; Jedrzejewski, K.P. Interferometric fiber Bragg gratings. In *Proc. SPIE*; Vol. 5576, pp. 37–41. https://doi.org/10.1117/12.581514.

125. Cheng, X.; Pecht, M. In Situ Stress Measurement Techniques on Li-ion Battery Electrodes: A Review. *Energies* **2017**, *10*, 591. https://doi.org/10.3390/en10050591.
126. Peng, J.; Zhou, X.; Jia, S.; Xu, S.; Chen, J. Design of a sensitivity-enhanced FBG strain sensor and its application in state estimation for lithium-ion battery. In Proceedings of the AOPC 2019: Optical Fiber Sensors and Communication; Zhang, J.; Fu, S.; Yang, J., Eds., Bellingham, Washington, USA, 2019; Proceedings of SPIE, p. 10. https://doi.org/10.1117/12.2539787.
127. Komma, J.; Schwarz, C.; Hofmann, G.; Heinert, D.; Nawrodt, R. Thermo-optic coefficient of silicon at 1550 nm and cryogenic temperatures. *Appl. Phys. Lett.* **2012**, *101*, 041905. https://doi.org/10.1063/1.4738989.
128. Kersey, A.D.; Davis, M.A.; Patrick, H.J.; LeBlanc, M.; Koo, K.P.; Askins, C.G.; Putnam, M.A.; Friebele, E.J. Fiber grating sensors. *Journal of Lightwave Technology* **1997**, *15*, 1442–1463. https://doi.org/10.1109/50.618377.
129. Novais, S.; Nascimento, M.; Grande, L.; Domingues, M.F.; Antunes, P.; Alberto, N.; Leitão, C.; Oliveira, R.; Koch, S.; Kim, G.T.; et al. Internal and External Temperature Monitoring of a Li-Ion Battery with Fiber Bragg Grating Sensors. *Sensors* **2016**, *16*. https://doi.org/10.3390/s16091394.
130. Alcock, K.M.; Grammel, M.; González-Vila, Á.; Binetti, L.; Goh, K.; Alwis, L.S. An accessible method of embedding fibre optic sensors on lithium-ion battery surface for in-situ thermal monitoring. *Sensors and Actuators A: Physical* **2021**, *332*, 113061. https://doi.org/10.1016/j.sna.2021.113061.
131. Unterkofler, J.; Glanz, G.; Koller, M.; Klambauer, R.; Bergmann, A. Strain Compensation Methods for Fiber Bragg Grating Temperature Sensors Suitable for Integration into Lithium-Ion Battery Electrolyte. *Batteries* **2023**, *9*, 34. https://doi.org/10.3390/batteries9010034.
132. Nascimento, M.; Ferreira, M.; Pinto, J. Simultaneous Sensing of Temperature and Bi-Directional Strain in a Prismatic Li-Ion Battery. *Batteries* **2018**, *4*, 23. https://doi.org/10.3390/batteries4020023.
133. Yang, G.; Leitão, C.; Li, Y.; Pinto, J.; Jiang, X. Real-time temperature measurement with fiber Bragg sensors in lithium batteries for safety usage. *Measurement* **2013**, *46*, 3166–3172. https://doi.org/10.1016/j.measurement.2013.05.027.
134. Sommer, L.W.; Raghavan, A.; Kiesel, P.; Saha, B.; Schwartz, J.; Lochbaum, A.; Ganguli, A.; Bae, C.J.; Alamgir, M. Monitoring of Intercalation Stages in Lithium-Ion Cells over Charge-Discharge Cycles with Fiber Optic Sensors. *J. Electrochem. Soc.* **2015**, *162*, A2664–A2669. https://doi.org/10.1149/2.0361514jes.
135. Rao, Y.J. In-fibre Bragg grating sensors. *Meas. Sci. Technol.* **1997**, *8*, 355–375. https://doi.org/10.1088/0957-0233/8/4/002.
136. Sommer, L.W.; Kiesel, P.; Ganguli, A.; Lochbaum, A.; Saha, B.; Schwartz, J.; Bae, C.J.; Alamgir, M.; Raghavan, A. Fast and slow ion diffusion processes in lithium ion pouch cells during cycling observed with fiber optic strain sensors. *J. Power Sources* **2015**, *296*, 46–52. https://doi.org/10.1016/j.jpowsour.2015.07.025.
137. Meyer, J.; Nedjalkov, A.; Doering, A.; Angelmahr, M.; Schade, W. Fiber optical sensors for enhanced battery safety. In Proceedings of the Fiber Optic Sensors and Applications XII; Pickrell, G.; Udd, E.; Du, H.H., Eds. SPIE, 2015, SPIE Proceedings, p. 94800Z. https://doi.org/10.1117/12.2183325.
138. Raghavan, A.; Kiesel, P.; Sommer, L.W.; Schwartz, J.; Lochbaum, A.; Hegyi, A.; Schuh, A.; Arakaki, K.; Saha, B.; Ganguli, A.; et al. Embedded fiber-optic sensing for accurate internal monitoring of cell state in advanced battery management systems part 1: Cell embedding method and performance. *J. Power Sources* **2017**, *341*, 466–473. https://doi.org/10.1016/j.jpowsour.2016.11.104.
139. Bae, C.J.; Manandhar, A.; Kiesel, P.; Raghavan, A. Monitoring the Strain Evolution of Lithium–Ion Battery Electrodes using an Optical Fiber Bragg Grating Sensor. *Energy Technol.* **2016**, *4*, 851–855. https://doi.org/10.1002/ente.201500514.
140. Nascimento, M.; Novais, S.; Ding, M.S.; Ferreira, M.S.; Koch, S.; Passerini, S.; Pinto, J.L. Internal strain and temperature discrimination with optical fiber hybrid sensors in Li-ion batteries. *J. Power Sources* **2019**, *410-411*, 1–9. https://doi.org/10.1016/j.jpowsour.2018.10.096.
141. Yu, Y.; Vincent, T.; Sansom, J.; Greenwood, D.; Marco, J. Distributed internal thermal monitoring of lithium ion batteries with fibre sensors. *J Energy Storage* **2022**, *50*, 104291. https://doi.org/10.1016/j.est.2022.104291.
142. Ghannoum, A.; Nieva, P. Graphite lithiation and capacity fade monitoring of lithium ion batteries using optical fibers. *J Energy Storage* **2020**, *28*, 101233. https://doi.org/10.1016/j.est.2020.101233.
143. Gardner, C.; Langhammer, E.; Du, W.; Brett, D.J.L.; Shearing, P.R.; Roberts, A.J.; Amietszajew, T. In-Situ Li-Ion Pouch Cell Diagnostics Utilising Plasmonic Based Optical Fibre Sensors. *Sensors* **2022**, *22*. https://doi.org/10.3390/s22030738.
144. Bonefacino, J.; Ghashghaie, S.; Zheng, T.; Lin, C.P.; Zheng, W.; Blanquer, L.A.; Huang, J.; Gervillié, C.; Tam, H.Y.; Tarascon, J.M.; et al. High-Fidelity Strain and Temperature Measurements of Li-Ion Batteries Using Polymer Optical Fiber Sensors. *J. Electrochem. Soc.* **2022**, *169*, 100508. https://doi.org/10.1149/1945-7111/ac957e.
145. Chen, D.; Zhao, Q.; Zheng, Y.; Xu, Y.; Chen, Y.; Ni, J.; Zhao, Y. Recent Progress in Lithium-Ion Battery Safety Monitoring Based on Fiber Bragg Grating Sensors. *Sensors* **2023**, *23*. https://doi.org/10.3390/s23125609.
146. Pietsch, P.; Hess, M.; Ludwig, W.; Eller, J.; Wood, V. Combining operando synchrotron X-ray tomographic microscopy and scanning X-ray diffraction to study lithium ion batteries. *Scientific reports* **2016**, *6*, 27994. https://doi.org/10.1038/srep27994.
147. Withers, P.J.; Bouman, C.; Carmignato, S.; Cnudde, V.; Grimaldi, D.; Hagen, C.K.; Maire, E.; Manley, M.; Du Plessis, A.; Stock, S.R. X-ray computed tomography. *Nature Reviews Methods Primers* **2021**, *1*. https://doi.org/10.1038/s43586-021-00015-4.
148. Maire, E.; Withers, P.J. Quantitative X-ray tomography. *International Materials Reviews* **2014**, *59*, 1–43. https://doi.org/10.1179/1743280413Y.0000000023.

149. Brunke, O.; Brockdorf, K.; Drews, S.; Müller, B.; Donath, T.; Herzen, J.; Beckmann, F. Comparison between x-ray tube-based and synchrotron radiation-based mCT. In Proceedings of the Developments in X-Ray Tomography VI; Stock, S.R., Ed. SPIE, 2008, SPIE Proceedings, p. 70780U. https://doi.org/10.1117/12.794789.
150. Brant, W.R.; Schmid, S.; Du, G.; Gu, Q.; Sharma, N. A simple electrochemical cell for in-situ fundamental structural analysis using synchrotron X-ray powder diffraction. *Journal of Power Sources* **2013**, *244*, 109–114. https://doi.org/10.1016/j.jpowsour.2013.03.086.
151. Su, L.; Choi, P.; Parimalam, B.S.; Litster, S.; Reeja-Jayan, B. Designing reliable electrochemical cells for operando lithium-ion battery study. *MethodsX* **2021**, *8*, 101562. https://doi.org/10.1016/j.mex.2021.101562.
152. Lim, J.; Li, Y.; Alsem, D.H.; So, H.; Lee, S.C.; Bai, P.; Cogswell, D.A.; Liu, X.; Jin, N.; Yu, Y.s.; et al. Origin and hysteresis of lithium compositional spatiodynamics within battery primary particles. *Science* **2016**, *353*, 566–571. https://doi.org/10.1126/science.aaf4914.
153. Borkiewicz, O.J.; Shyam, B.; Wiaderek, K.M.; Kurtz, C.; Chupas, P.J.; Chapman, K.W. The AMPIX electrochemical cell: a versatile apparatus for in situ X-ray scattering and spectroscopic measurements. *J Appl Crystallogr* **2012**, *45*, 1261–1269. https://doi.org/10.1107/S0021889812042720.
154. Bond, T.; Zhou, J.; Cutler, J. Electrode Stack Geometry Changes during Gas Evolution in Pouch-Cell-Type Lithium Ion Batteries. *J. Electrochem. Soc.* **2017**, *164*, A6158–A6162. https://doi.org/10.1149/2.0241701jes.
155. Beattie, S.D.; Larcher, D.; Morcrette, M.; Simon, B.; Tarascon, J.M. Si Electrodes for Li-Ion Batteries—A New Way to Look at an Old Problem. *J. Electrochem. Soc.* **2008**, *155*, A158. https://doi.org/10.1149/1.2817828.
156. Obrovac, M.N.; Krause, L.J. Reversible Cycling of Crystalline Silicon Powder. *J. Electrochem. Soc.* **2007**, *154*, A103. https://doi.org/10.1149/1.2402112.
157. Fister, T.T.; Goldman, J.L.; Long, B.R.; Nuzzo, R.G.; Gewirth, A.A.; Fenter, P.A. X-ray diffraction microscopy of lithiated silicon microstructures. *Appl. Phys. Lett.* **2013**, *102*. https://doi.org/10.1063/1.4798554.
158. Wang, X.; Sone, Y.; Kuwajima, S. In Situ Investigation of the Volume Change in Li-ion Cell with Charging and Discharging. *J. Electrochem. Soc.* **2004**, *151*, A273. https://doi.org/10.1149/1.1635827.
159. Finegan, D.P.; Scheel, M.; Robinson, J.B.; Tjaden, B.; Di Michiel, M.; Hinds, G.; Brett, D.J.L.; Shearing, P.R. Investigating lithium-ion battery materials during overcharge-induced thermal runaway: an operando and multi-scale X-ray CT study. *Physical chemistry chemical physics* **2016**, *18*, 30912–30919. https://doi.org/10.1039/c6cp04251a.
160. Trease, N.M.; Ko ster, T.K.J.; Grey, C.P. In Situ NMR Studies of Lithium Ion Batteries. *Interface magazine* **2011**, *20*, 69–73. https://doi.org/10.1149/2.F07113if.
161. Le Houx, J.; Kramer, D. X-ray tomography for lithium ion battery electrode characterisation — A review. *Energy Reports* **2021**, *7*, 9–14. https://doi.org/10.1016/j.egyr.2021.02.063.
162. Zhou, H.; An, K.; Allu, S.; Pannala, S.; Li, J.; Bilheux, H.Z.; Martha, S.K.; Nanda, J. Probing Multiscale Transport and Inhomogeneity in a Lithium-Ion Pouch Cell Using In Situ Neutron Methods. *ACS Energy Letters* **2016**, *1*, 981–986. https://doi.org/10.1021/acsenergylett.6b00353.
163. Calzada, E.; Schillinger, B.; Grünauer, F. Construction and assembly of the neutron radiography and tomography facility ANTARES at FRM II. *Nuclear Instruments and Methods in Physics Research Section A: Accelerators, Spectrometers, Detectors and Associated Equipment* **2005**, *542*, 38–44. https://doi.org/10.1016/j.nima.2005.01.009.
164. Clerici, D.; Mocera, F.; Somà, A. Electrochemical–mechanical multi-scale model and validation with thickness change measurements in prismatic lithium-ion batteries. *J. Power Sources* **2022**, *542*, 231735. https://doi.org/10.1016/j.jpowsour.2022.231735.
165. Rieger, B.; Schuster, S.F.; Erhard, S.V.; Osswald, P.J.; Rheinfeld, A.; Willmann, C.; Jossen, A. Multi-directional laser scanning as innovative method to detect local cell damage during fast charging of lithium-ion cells. *J. Energy Storage* **2016**, *8*, 1–5. https://doi.org/10.1016/j.est.2016.09.002.
166. Yang, H.; Tao, W.; Zhang, Z.; Zhao, S.; Yin, X.; Zhao, H. Reduction of the Influence of Laser Beam Directional Dithering in a Laser Triangulation Displacement Probe. *Sensors* **2017**, *17*. https://doi.org/10.3390/s17051126.
167. Ding, D.; Ding, W.; Huang, R.; Fu, Y.; Xu, F. Research progress of laser triangulation on-machine measurement technology for complex surface: A review. *Measurement* **2023**, *216*, 113001. https://doi.org/10.1016/j.measurement.2023.113001.
168. Kienle, P.; Batarilo, L.; Akgül, M.; Köhler, M.H.; Wang, K.; Jakobi, M.; Koch, A.W. Optical Setup for Error Compensation in a Laser Triangulation System. *Sensors* **2020**, *20*. https://doi.org/10.3390/s20174949.
169. Zhao, H.; Wang, Z.; Jia, G.; Li, X.; Zhang, Y. Field imaging system for hyperspectral data, 3D structural data and panchromatic image data measurement based on acousto-optic tunable filter. *Optics express* **2018**, *26*, 17717–17730. https://doi.org/10.1364/OE.26.017717.
170. Bohn, G.; Taub, J.; Linke, A.; Bayer, S.; Oeser, D.; Ziegler, A.; Ettl, P.; Ackva, A. High-resolution Interferometric Measurement of Thickness Change on a Lithium-Ion Pouch Battery. *IOP Conf. Ser.: Earth Environ. Sci.* **2019**, *281*, 012030. https://doi.org/10.1088/1755-1315/281/1/012030.
171. Bohn, G.; Taub, J.; Oeser, D.; Ziegler, A.; Gielinger, S. Fast and High Resolution Expansion Measurement at an Audi e-tron Battery Cell. In Proceedings of the 2022 IEEE Vehicle Power and Propulsion Conference (VPPC). IEEE, 2022, pp. 1–6. https://doi.org/10.1109/VPPC55846.2022.10003340.
172. Xu, Z.; Shilpiekandula, V.; Youcef-toumi, K.; Yoon, S.F. White-light scanning interferometer for absolute nano-scale gap thickness measurement. *Optics express* **2009**, *17*, 15104–15117. https://doi.org/10.1364/OE.17.015104.

173. Lehmann, P.; Tereschenko, S.; Xie, W. Fundamental aspects of resolution and precision in vertical scanning white-light interferometry. *Surf. Topogr.: Metrol. Prop.* **2016**, *4*, 024004. https://doi.org/10.1088/2051-672X/4/2/024004.
174. Krause, T.J.H. Self-witnessing coherent imaging for automatic noise filtering and artifact removal in laser process monitoring. Thesis, Queen's University, Kingston, Ontario, Canada, 2022.
175. Yang, K.; Sheng, Z.; Chen, B.; Li, X.; Fu, Y. Dual-surface li-ion battery deformation measurement by temporal electronic speckle pattern interferometry. In Proceedings of the International Conference on Optical and Photonic Engineering (icOPEN 2022); Zuo, C.; Wang, H.; Feng, S.; Kemao, Q., Eds. SPIE, 24.11.2022 - 27.11.2022, p. 94. https://doi.org/10.1117/12.2667169.
176. Yang, L.; Xie, X.; Zhu, L.; Wu, S.; Wang, Y. Review of electronic speckle pattern interferometry (ESPI) for three dimensional displacement measurement. *Chin. J. Mech. Eng.* **2014**, *27*, 1–13. https://doi.org/10.3901/CJME.2014.01.001.
177. Zhang, Z.; Towers, C.E.; Towers, D.P. Time efficient color fringe projection system for 3D shape and color using optimum 3-frequency Selection. *Optics express* **2006**, *14*, 6444–6455. https://doi.org/10.1364/OE.14.006444.
178. Griffin, P.M.; Narasimhan, L.S.; Yee, S.R. Generation of uniquely encoded light patterns for range data acquisition. *Pattern Recognition* **1992**, *25*, 609–616. https://doi.org/10.1016/0031-3203(92)90078-W.
179. van der Jeught, S.; Dirckx, J.J.J. Deep neural networks for single shot structured light profilometry. *Optics express* **2019**, *27*, 17091–17101. https://doi.org/10.1364/OE.27.017091.
180. Geng, J. Structured-light 3D surface imaging: a tutorial. *Adv. Opt. Photon.* **2011**, *3*, 128. https://doi.org/10.1364/AOP.3.000128.
181. Ishii, I.; Yamamoto, K.; Doi, K.; Tsuji, T. High-speed 3D image acquisition using coded structured light projection. In Proceedings of the 2007 IEEE/RSJ International Conference on Intelligent Robots and Systems. IEEE, 2007, pp. 925–930. https://doi.org/10.1109/IROS.2007.4399180.
182. Wang, Z. Review of real-time three-dimensional shape measurement techniques. *Measurement* **2020**, *156*, 107624. https://doi.org/10.1016/j.measurement.2020.107624.
183. Pan, B.; Qian, K.; Xie, H.; Asundi, A. Two-dimensional digital image correlation for in-plane displacement and strain measurement: a review. *Meas. Sci. Technol.* **2009**, *20*, 062001. https://doi.org/10.1088/0957-0233/20/6/062001.
184. Salvi, J.; Fernandez, S.; Pribanic, T.; Llado, X. A state of the art in structured light patterns for surface profilometry. *Pattern Recognition* **2010**, *43*, 2666–2680. https://doi.org/10.1016/j.patcog.2010.03.004.
185. Schreier, H.; Orteu, J.J.; Sutton, M.A. *Image Correlation for Shape, Motion and Deformation Measurements*; Springer US: Boston, MA, 2009. https://doi.org/10.1007/978-0-387-78747-3.
186. Gao, Y.; Cheng, T.; Su, Y.; Xu, X.; Zhang, Y.; Zhang, Q. High-efficiency and high-accuracy digital image correlation for three-dimensional measurement. *Optics and Lasers in Engineering* **2015**, *65*, 73–80. https://doi.org/10.1016/j.optlaseng.2014.05.013.
187. Pan, B. Digital image correlation for surface deformation measurement: historical developments, recent advances and future goals. *Meas. Sci. Technol.* **2018**, *29*, 082001. https://doi.org/10.1088/1361-6501/aac55b.
188. Boukhtache, S.; Abdelouahab, K.; Berry, F.; Blaysat, B.; Grédiac, M.; Sur, F. When Deep Learning Meets Digital Image Correlation. *Optics and Lasers in Engineering* **2021**, *136*, 106308. https://doi.org/10.1016/j.optlaseng.2020.106308.
189. Wang, G.; Zhang, L.; Yao, X. StrainNet-3D: Real-time and robust 3-dimensional speckle image correlation using deep learning. *Optics and Lasers in Engineering* **2022**, *158*, 107184. https://doi.org/10.1016/j.optlaseng.2022.107184.
190. Luo, J.; Dai, C.Y.; Wang, Z.; Liu, K.; Mao, W.G.; Fang, D.N.; Chen, X. In-situ measurements of mechanical and volume change of LiCoO2 lithium-ion batteries during repeated charge–discharge cycling by using digital image correlation. *Measurement* **2016**, *94*, 759–770. https://doi.org/10.1016/j.measurement.2016.09.023.
191. Leung, P.K.; Moreno, C.; Masters, I.; Hazra, S.; Conde, B.; Mohamed, M.R.; Dashwood, R.J.; Bhagat, R. Real-time displacement and strain mappings of lithium-ion batteries using three-dimensional digital image correlation. *J. Power Sources* **2014**, *271*, 82–86. https://doi.org/10.1016/j.jpowsour.2014.07.184.
192. Mutscheller, A. Safety Standards of Protection against X-ray Dangers. *Radiology* **1928**, *10*, 468–476. https://doi.org/10.1148/10.6.468.
193. Keshavamurthy, R.S.; Kumar, D.S. Radiation safety and radiation shielding design. In *Physics of Nuclear Reactors*; Elsevier, 2021; pp. 635–694. https://doi.org/10.1016/B978-0-12-822441-0.00009-1.
194. Bilderback, D.H.; Elleaume, P.; Weckert, E. Review of third and next generation synchrotron light sources. *Journal of Physics B: Atomic, Molecular and Optical Physics* **2005**, *38*, S773–S797. https://doi.org/10.1088/0953-4075/38/9/022.